2019-08

Cyclostationary Signal Detection and Doppler Rate Correction for LEO Nanosatellites in the ISM Band

Hofmann, Jonas

Monterey, California. Naval Postgraduate School

NPS-SP-19-002

NAVAL POSTGRADUATE SCHOOL

MONTEREY, CALIFORNIA

CYCLOSTATIONARY SIGNAL DETECTION AND DOPPLER RATE CORRECTION FOR LEO NANOSATELLITES IN THE ISM BAND

by

Jonas Hofmann

August 2019

THIS PAGE INTENTIONALLY LEFT BLANK

REPORT DOCUMENTATION PAGE

Form Approved
OMB No. 0704-0188

1. REPORT DATE *(DD-MM-YYYY)*	**2. REPORT TYPE**	**3. DATES COVERED** *(From-To)*
August 2019	Master's Thesis/Technical Report	15 Feb 2019 to 15 Aug 2019

4. TITLE AND SUBTITLE
Cyclostationary Signal Detection and Doppler Rate Correction for LEO Nanosatellites in the ISM Band

5a. CONTRACT NUMBER

5b. GRANT NUMBER

5c. PROGRAM ELEMENT NUMBER

6. AUTHOR(S)
Jonas Hofmann

5d. PROJECT NUMBER

5e. TASK NUMBER

5f. WORK UNIT NUMBER

7. PERFORMING ORGANIZATION NAME(S) AND ADDRESS(ES) AND ADDRESS(ES)
Naval Postgraduate School Monterey,
CA 93943-5000

8. PERFORMING ORGANIZATION REPORT NUMBER
NPS-SP-19-002

9. SPONSORING / MONITORING AGENCY NAME(S) AND ADDRESS(ES)
Universität der Bundeswehr München
Fakultät für Elektrotechnik
Institut für Informationstechnik
Werner-Heisenberg-Weg 39
85579 Neubiberg

10. SPONSOR/MONITOR'S ACRONYM(S)

11. SPONSOR/MONITOR'S REPORT NUMBER(S)

12. DISTRIBUTION / AVAILABILITY STATEMENT
Approved for public release; distribution is unlimited

13. SUPPLEMENTARY NOTES

14. ABSTRACT

The Space Systems Academic Group (SSAG) of the Naval Postgraduate School (NPS) is a pioneer in the development of nanosatellites. While their miniature size promises great possibilities for applications and research, it also poses severe challenges on the communications link.

The SSAG operates satellites called PropCube. Often PropCube's signal cannot be demodulated successfully due to high interference in the industrial, scientific and medical (ISM) band and Doppler shifts occurring in the satellite downlink. In this case, it is useful to have the more general information whether the satellite's signal is present or not. Moreover, in the next step towards demodulation, the frequency offset must be corrected.

In this thesis, a detector is build, which exploits cyclostationary signal characteristics to reliably detect PropCube's GFSK signal in the ISM environment. If the satellite's signal is detected, the position of cyclic features in the frequency domain reveal the Doppler offset, which can then be removed. A performance analysis demonstrating the effectiveness of the proposed algorithm is conducted.

15. SUBJECT TERMS
satellite communication, SATCOM, nano satellites, cube satellites, CubeSats, PropCube, cyclostationarity, spectral correlation, signal detection, Doppler shift, Doppler rate, Doppler offset, software-defined radio, SDR, ISM, WGN

16. SECURITY CLASSIFICATION OF:			**17. LIMITATION OF ABSTRACT**	**18. NUMBER OF PAGES**	**19a. NAME OF RESPONSIBLE PERSON**
a. REPORT	**b. ABSTRACT**	**c. THIS PAGE**			**19b. TELEPHONE NUMBER** *(include area code)*
Unclassified	Unclassified	Unclassified		61	

Standard Form 298 (Rev. 8-98)
Prescribed by ANSI Std. Z39.18

THIS PAGE INTENTIONALLY LEFT BLANK

NAVAL POSTGRADUATE SCHOOL
Monterey, California 93943-5000

Ann E. Rondeau
President

Steven R. Lerman
Provost

The report entitled *Cyclostationary Signal Detection and Doppler Rate Correction for LEO Nanosatellites in the ISM Band* was prepared for *Universität der Bundeswehr München* and funded by the *German Armed Forces*.

Further distribution of all or part of this report is authorized.

This report was prepared by:

_____
Jonas Hofmann
Lieutenant, German Air Force

Reviewed by:

_____
James Newman
Chair Space Systems Academic Group

Released by:

_____
Jeffrey D. Paduan
Dean of Research

Acknowledgements

This page is dedicated to my teachers and motivators, who enabled me to write this thesis.

Cyclic spectral analysis is a particularly challenging subject in the wide field of signal processing. Getting in touch with it for the first time was as a working student for a German company called *Rohde & Schwarz*, seeking for suitable methods to classify RF signals of commercial drones. Online searches usually refer to books of Gardner and papers published by a handful of scientists working in the small cyclostationary community. But there was one rather unconventional result, an online blog [1], where a researcher explained the concepts of cyclostationarity in a vivid manner, always minding the practical application of all theory. A few months later, working on a signal detection problem, it turns out that its author, Chad M. Spooner, works for a company based in Monterey, CA. From the first meeting on, Chad put great effort in supporting me in my understanding of cyclostationarity, even if he was not affiliated with NPS or my project. In weekly sessions, Chad took time to explain concepts, common mistakes and implementational aspects, despite an overfull calendar. Moreover, he motivated me to pursue certain paths a little further, which was often the last step leading to great results. Eventually, he declared himself willing to become the co-advisor of this thesis. Thank you, Chad, for putting so much work in this project!

The possibility to write my master thesis at NPS was first proposed by Professor Andreas Knopp. Over many months of application process on both, the German and the American side, he was a tremendous promoter of this exchange, knowing about the great opportunities of working on the communication link of real-world satellites. The successful accomplishment of my stay in Monterey while being able to work in such an interesting environment is majorly based on his commitment. In the past years, I experienced him to be an excellent mentor, who taught me digital signal processing from scratch. Having him on my side was helpful in countless situations, providing guidance in technical question via WebEx-meetings at times long after most people in Germany have finished their dinner. It is hard to believe that I could have learned in Germany as much as I did in Monterey in the past six months. Therefore, I am very glad to be a student of yours!

Last but not least, I would like to express my appreciation for a group of very committed people in the Space Systems Academic Group at NPS: Michael Matthews, an absolute pundit in the field of signal processing, who often supported me in my research and took initiative to introduce me to Chad. Professor Emeritus Rudolph Panholzer, who puts great effort in coordinating the exchange on the American side. Giovanni Minelli, who taught me fundamentals in orbital mechanics and introduced me to the communication design of PropCube. Dr. James Newman, who fosters the exchange program and takes time to provide the possibilities needed for a successful work environment.

Contents

List of Figures

List of Abbreviations

ACF Autocorrelation Function 10–12

AWGN Additive White Gaussian Noise 17, 55

AX.25 Data Link Layer Protocol 30

CACF Cyclic Autocorrelation Function 12, 13, 24

COF Spectral Coherence Function 15, 16, 19, 29, 31

CPM Continuous-Phase Modulation 14, 23–25

CRC Cyclic Redundany Check 30

DFT Discrete Fourier Transform 19, 29–31, 36–39, 50, 53, 60, 61

GFSK Gaussian Frequency Shift Keying 14, 16, 21, 23, 25, 30–32, 34, 35, 45, 47, 53

ISM industrial, scientific and medical 7–9, 29, 30, 34, 42, 44–46, 48, 50, 53

LEO Low Earth Orbit 8, 37, 50

NPS Naval Postgraduate School 7

NRZI Non Return to Zero inverted 30

PSD Power Spectral Density 12–14, 16, 17, 19

ROC Receiver Operating Characteristics 8, 9, 45

SCF Spectral Correlation Function 12–21, 23–26, 28, 29, 31, 32, 36

SNR Signal-to-Noise ratio 7, 16, 31, 40, 42, 45–48, 54, 55

SSAG Space Systems Academic Group 7, 29

TSM Time Smoothing Method 19, 20, 31, 35, 38, 58, 60

WGN White Gaussian Noise 9, 17, 29, 31, 34, 38–40, 44, 45, 47, 54, 60, 61

1. Introduction and Motivation

1.1. Motivation

The Space Systems Academic Group (SSAG) of the Naval Postgraduate School (NPS) in Monterey, CA, is a pioneer in the development nanosatellites. So far, three satellites built to CubeSat specifications have been launched: Flora, Fauna and Merryweather. Those satellites are referred to as PropCubes, which is the SSAG CubeSat implementation.

The miniature size of those nanosatellites promises great possibilities for applications and research but also poses severe challenges on all fields of engineering. For example in communication engineering, the small satellite size implies tiny solar panels, which lead to little transmit power. The Signal-to-Noise ratio (SNR) was estimated to be in a range from $-2dB$ to $13dB$ when no additional interference is present, depending on the distance to the ground station, which varies greatly in the course of an overflight. This change of distance also causes the well known phenomena of Doppler shift in frequency, and the change of Doppler shift over time introduces the so called Doppler rate. For CubeSats transmitting at $914MHz$, which are usually in a low-earth orbit (LEO), the Doppler shift causes a frequency deviation up to $24KHz$ and the Doppler rate is as high as $310\frac{Hz}{s}$ at its peak. The already difficult communication task is complicated by design decisions of PropCube: Following the CubeSat philosophy, the communication link was chosen to be in an industrial, scientific and medical (ISM) band. The benefit that the ISM band is allowed to be used for free is countered by the fact that strong interference occurs. For example, there are radars, remote controlled drones and car-openers operating at the same frequency. Despite the directional characteristics of the ground station's antenna, interference exceeding the satellite's signal by over $37dB$ is present in signal recordings. This might happen for example at an early stage in an overflight when the antenna is pointed almost horizontally and a CubeSat has to compete with a car-opener at a parking lot nearby or if an airborne radar is pointed towards the antennas main lobe. Appendix A provides an overview of spectrograms of typical bursts, which illustrates the interfering environment, and the method used for estimating the SNR values is explained.

Often, the satellite's signal can not be demodulated and decoded successfully. In that case, it is useful to have the more general information whether the satellite is still transmitting or not. Prior projects focused on implementing an energy-based signal detector, known as radiometer. Gardner [2] showed that the radiometer is an optimum detector, following a Maximum-Likelihood approach, assuming a stationary noise level. Due to

the vast variations of noise- and signal-power, as well as strong interference discussed in the previous paragraph, it is hard to find a suitable energy threshold which yields an acceptable trade-off between detection probability and false alarm probability, known as Receiver Operating Characteristics (ROC). This dilemma is discussed in more detail in Appendix B. Since the radiometer is only an energy-detector, any interference with a sufficient amount of energy could raise a false alarm. In a challenging environment like the ISM band, another class of detectors can outperform the radiometer by far: Cycle detectors, originally proposed by Gardner in [2], exploit cyclostationary features of communications signals and are considered to be tolerant against interference. Moreover, Gardner and Spooner [3] show performance advantages of cycle detectors over radiometers.

The novelty of this thesis lies in the application of cycle detectors to signals that are corrupted by a high Doppler rate. Since the measurement of cyclic features relies on the signal's consistency in the frequency domain, the Doppler rate tends to make cyclic spectral analysis a less promising approach. However, in this thesis it is demonstrated that such methods, which are well known to perform great for terrestrial blind signal detection and classification, can successfully be applied to LEO satellites and perform reliably under strong interference. An algorithm is proposed that uses an adaptive decision statistic and best-performing parameter settings are discussed.

1.2. Thesis Structure

In order to properly discuss cycle detectors, Chapter 2 introduces the fundamentals of cyclic spectral analysis. The author paid great attention to start the development of the theory at points that are assumed to be well known to the readership. To present this mathematical part as vividly as possible, many simple examples are presented. Throughout the entire chapter, parallels from the so called conventional world, referring to conventional spectral analysis, to the cyclostationary world are drawn. At this point, advantages of cyclic spectral analysis become clear, which are then discussed in Section 2.1.4. While the analytical derivation of cyclic functions is a theoretical construct, Section 2.2 briefly introduces a practical estimation method and its implementational aspects. Eventually, Section 2.3 summarizes the detection statistic of cycle detectors.

Chapter 3 is the most mathematically rigorous part of this thesis. The ideal spectral correlation function for Procube's communication design is derived by the application of a paper by Napolitano and Spooner [4]. This effort is taken to justify estimation results by analytical means and to develop a modified cycle detector for this specific signal type.

The theoretical foundation is used in Chapter 4 to design a detection statistic more suitable for the ISM environment. Different approaches are discussed and explanations

for the final design decision are provided. Moreover, Chapter 4 contains a key element necessary for the application of cyclic spectral analysis to Doppler rate corrupted signals: The adequate choice of observation time (later on referred to as block length), to avoid smearing of cyclic features. To guarantee residual smearing to be within certain bounds, design parameters are introduced in Section 4.2.3. Eventually, the detector, which operates on a single observation time must be applied to a continuous stream of samples. A strategy, that meets a trade-off between computational tractability and resolution in the time domain, is presented in Section 4.4.1 and its result is used in Section 4.4.2 to correct frequency offsets.

Equipped with this algorithm, Chapter 5 evaluates its performance in different scenarios: A simulator was implemented to determine the probability of detection in WGN and an approach is presented to estimate the ROC in the ISM environment. Finally, the detectors performance is tested in Section 5.4 on real-world data from a PropCube overflight.

2. Introduction to Second Order Cyclic Spectral Analysis

In this chapter, fundamental ideas of the theory of cyclic spectral analysis are introduced. Without loss of generality, the term *stationary* refers to stationarity in the wide sense. If stationarity in the strict sense is considered, it is specifically mentioned. Definitions for both, strict- and wide-sense stationarity are provided in [5].

2.1. Theory of Cyclostationarity

2.1.1. Cyclic Autocorrelation Function

The starting point for the development of the cyclostationary framework in this thesis is the conventional autocorrelation function (ACF) for stationary signals, which is assumed to be well known to the readership:

$$R_x(\tau) = \lim_{T\to\infty} \frac{1}{T} \int_{-T/2}^{T/2} x(t+\tau/2)x^*(t-\tau/2)dt, \tag{2.1}$$

where the star-operator * denotes the complex conjugate. A stationary signal model is adequate for most communication signals if the observation time exceeds many symbols and if the signal is considered to be sampled at the symbol rate after a matched filter. If the observation time decreases to the magnitude of a few symbols and an oversampled signal is considered, it becomes obvious that the stationary model no longer holds, as the following example illustrates.

Considering a simple Pulse-Amplitude-Modulated Signal, where the pulse shaping is a half-sine wave, a possible pulse train could look like $s(t)$ in Figure 2.1.

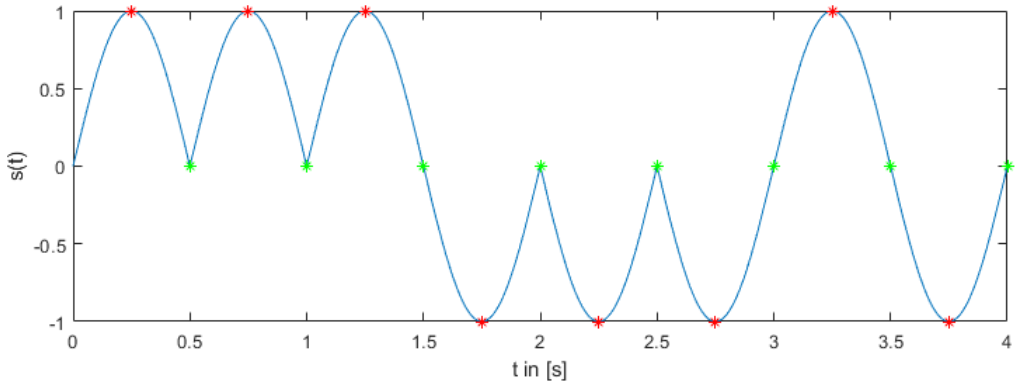

Figure 2.1.: PAM Pulsetrain with half-sine Pulse Shaping

If the sampling points are only at the red marks, which corresponds to an ideal sampling at Nyquist frequency, the sample sequence is stationary, assuming the data symbols are independent and identically distributed. In this case, it is easy to see that the expectation value of the sampling sequence is 0 and the variance is 1. If the sampling changes and the green marks are also considered to be sampling points, the sampling sequence can no longer be seen as stationary, since the variance of the green sampling points is 0. However, the sampling sequence can be seen as cyclostationary, since the variance changes periodically from sample to sample. To calculate the autocorrelation function of such a sequence, it is necessary to use a different approach.

The general form of the conventional ACF, applying to all non-stationary signals, is given by

$$R_x(t,\tau) = E\{x(t+\tau/2)x^*(t-\tau/2)\}, \tag{2.2}$$

where $E[.]$ is the expectation operator. Assuming that 2.2 contains a periodic behaviour, for example due to pulse-shaping effects like in the above example, Fourier coefficients can be determined by calculating

$$R_x^\alpha(\tau) = \lim_{T\to\infty} \frac{1}{T} \int_{-T/2}^{T/2} R_x(t,\tau) e^{-i2\pi\alpha t}\, dt, \tag{2.3}$$

where α represents one Fourier frequency, which is referred to as cycle frequency in the cyclostationary context. If a specific cycle frequency is present in equation 2.2, then the Fourier coefficient 2.3 will differ from zero. By taking all cycle frequencies into account, equation 2.2 can be expressed as a Fourier series

$$R_x(t,\tau) = \sum_{\alpha} R_x^{\alpha}(\tau) e^{i2\pi\alpha t}. \tag{2.4}$$

This shows the relationship between the conventional ACF $R_x(t,\tau)$ and the cyclic autocorrelation function $R_x^{\alpha}(\tau)$ (CACF). Moreover, the conventional ACF for stationary signals, equation 2.1, can be seen as a special case of the CACF, evaluted for $\alpha = 0$:

$$R_x^0(\tau) = \lim_{T\to\infty} \frac{1}{T} \int_{-T/2}^{T/2} R_x(t,\tau) e^{-i2\pi 0t}\, dt = R_x(\tau). \tag{2.5}$$

The fact that conventional formulas turn out to be special cases of cyclostationary approaches continues throughout this chapter.

A signal exhibits second-order cyclostationarity if there exist at at least one cycle frequencies $\alpha \neq 0$ with $R_x^{\alpha}(\tau) \neq 0$ [6]. This is related to the fact that the ACF and CACF are lag products of second order.

2.1.2. Spectral Correlation Function

The *Wiener relation*, which is again assumed to be well known to the readership, states that the Fourier transform of the conventional ACF of a stationary signal yields its power spectral density (PSD):

$$S(f) = \lim_{T\to\infty} \int_{-\frac{T}{2}}^{+\frac{T}{2}} R_x(\tau) e^{-i2\pi f\tau} d\tau. \tag{2.6}$$

Analogous, the *cyclic Wiener relation* states that the Fourier transform of the CACF yields a function known as the spectral correlation function SCF [7], which is of great importance to this thesis:

$$S_x^{\alpha}(f) = \lim_{T\to\infty} \int_{-\frac{T}{2}}^{+\frac{T}{2}} R_x^{\alpha}(\tau) e^{-i2\pi f\tau} d\tau. \tag{2.7}$$

Additionally, the PSD can also be calculated by evaluation of

$$S_x(f) = \lim_{T\to\infty} \lim_{U\to\infty} \frac{1}{U} \int_{-U/2}^{U/2} I_T(t,f) dt, \tag{2.8}$$

where

$$I_T(t,f) = \frac{1}{T} |X_T(t,f)|^2 \tag{2.9}$$

is known as the conventional periodogram, hence $X_T(t,f)$ is the Fourier transform of the signal defined by

$$X_T(t,f) = \int_{t-T/2}^{t+T/2} x(v)e^{-i2\pi f v}dv. \tag{2.10}$$

In strong analogy to the definition of the PSD via the periodogram, it is shown in [7] that the SCF is also defined by

$$S_x^\alpha(f) = \lim_{T\to\infty}\lim_{U\to\infty}\frac{1}{U}\int_{-U/2}^{U/2} I_T^\alpha(t,f)dt \tag{2.11}$$

where

$$I_T^\alpha(t,f) = \frac{1}{T}X_T(t,f+\alpha/2)X_T^*(t,f-\alpha/2) \tag{2.12}$$

is known as the cyclic periodogram. It follows, that the conventional periodogram turns out to be a special case of the cyclic periodogram for $\alpha = 0$

$$I_T^0(t,f) = \frac{1}{T}X_T(t,f)X_T^*(t,f) = \frac{1}{T}|X_T(t,f)|^2 = I_T(t,f) \tag{2.13}$$

and consequently the PSD is a special case of the SCF for $\alpha = 0$

$$S_x^0(f) = \lim_{T\to\infty}\lim_{U\to\infty}\frac{1}{U}\int_{-U/2}^{U/2} I_T^0(t,f)dt = \lim_{T\to\infty}\lim_{U\to\infty}\frac{1}{U}\int_{-U/2}^{U/2} I_T(t,f)dt = S_x(f). \tag{2.14}$$

The multiplication operation in equation 2.12, which defines the cyclic periodogram, can simply be interpreted as a correlation of two frequency components $f + \alpha/2$ and $f - \alpha/2$ for a snapshot of time T. Therefore, the SCF can be interpreted as the correlation function of those frequency components over time t. The link between cyclostationarity in the time-domain signal and spectral correlation in the frequency domain is given in equation 2.7: If cycle frequencies other than $\alpha = 0$ are present in the CACF $R_x^\alpha(\tau)$ due to cyclostationarity in the time domain, then there exist values $S_x^\alpha(f) \neq 0$, for $\alpha \neq 0$. This means, there are contributions in the SCF besides the PSD, which can be interpreted as correlation of spectral components due to equation 2.11.

The importance of the SCF and the cyclostationary framework in general arises from the fact that most man-made communication signals exhibit cyclostationarity. The exploitation of it yields significant advantages over conventional spectral analysis for signal detection and classification, as well as for many other applications. A brief discussion of those is given in Section 2.1.4.

Great effort has been put in the determination of analytic expressions for SCFs for various types of modulations. Gardner et. al. focus in [8] on real signals only and provide those for a selection of common communication signals. Nevertheless, for most modulation types, especially in the complex baseband representation, an analytic expression for the exact SCF is often unknown. An interesting approach was taken by Napolitano and Spooner in [4]. It is shown that close approximations or even the exact SCF, depending on the type of continuous-phase modulation (CPM), can be calculated by using the Laurent representation of CPM signals. Chapter 3 is dedicated to the application of this paper to the GFSK signal of PropCube.

In the following, the term α-slice refers to a slice of the SCF for a fixed value of cycle frequency α and a variable center frequency f. For example, the α-slice for $\alpha = 0$ coincides with the PSD.

Example: Figure 2.2 shows the SCF for PropCube's GFSK signal, which will be derived in detail in Chapter 3. With a modulation index of $h = 1$ *and a symbol rate of* $9600\frac{symbols}{s}$, *the signal contains two tones at* $\pm 4.8kHz$, *which can be observed clearly in the PSD at* $\alpha = 0$. *Moreover, strong cyclic features can be observed at the discrete cycle frequencies* $\alpha = \pm 9.6kHz$, *consisting of a tone and a lobe-like component, and much weaker ones at* $\alpha = \pm 19.2kHz$, *consisting only of a lobe-like component.*

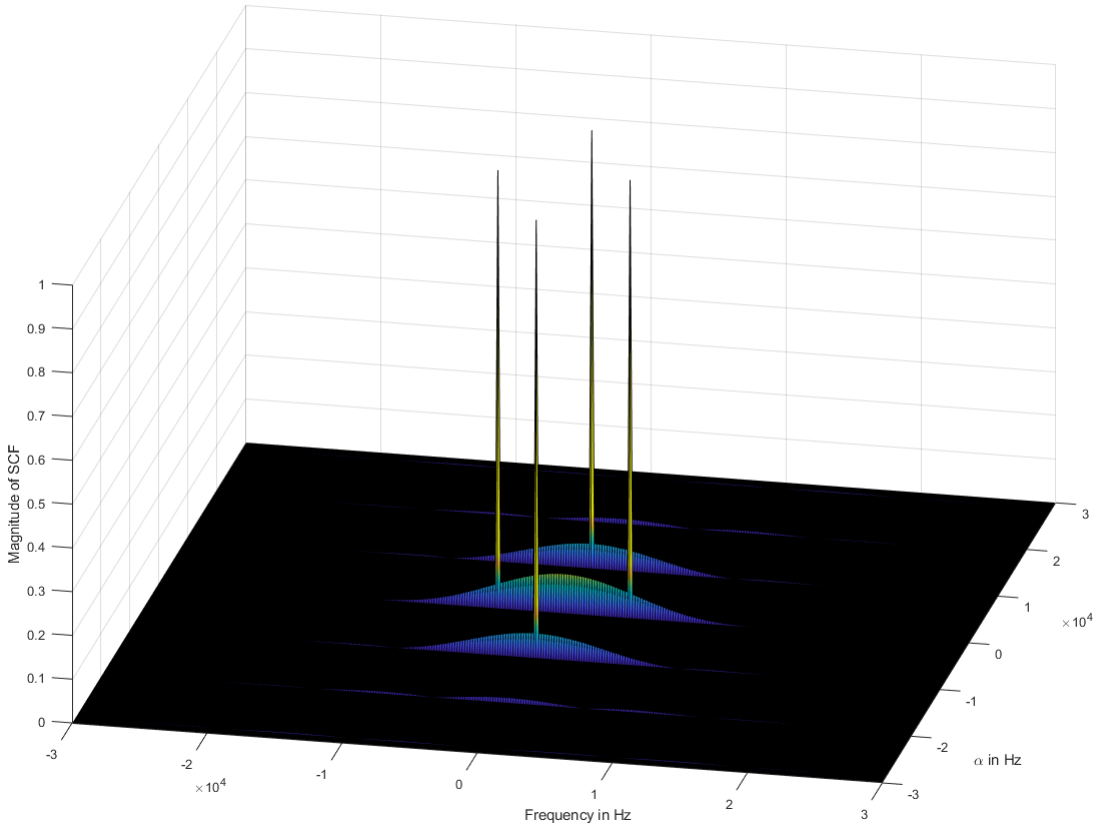

Figure 2.2.: SCF of a GFSK Signal

2.1.3. Spectral Coherence Function

The SCF yields the amount of spectral correlation present in a signal. As the signal power changes, the level of the SCF is affected. This implies complications on thresholding problems. One possible solution is to use the Spectral Coherence Function (COF) instead:

$$C_x^\alpha(f) = \frac{S_x^\alpha(f)}{\left[S_x^0(f+\alpha/2)S_x^0(f-\alpha/2)\right]^{1/2}}. \tag{2.15}$$

The COF normalizes each point of the SCF with the power present in the frequency bands that are correlated for this specific point. Therefore, the range of possible values of the magnitude of the COF is bound to the interval $[0,1]$. The entire α-slice at $C_x^0(f)$ is consequently normalized to one and referred to as *noise wall*.

A noiseless signal has in general lower energy, the further the frequency is separated from the center frequency. But this little energy still exhibits spectral correlation and is greatly upscaled in the COF, so that it leads to values close to one. Hence, the COF is

a useful tool when a substantial amount of noise is present, but a less favorable option for signals at very high SNR.

Example: Figure 2.3 shows the estimated COF of a simulated GFSK signal at an SNR of 3dB. The noise wall as well as cyclic features are clearly visible. When comparing this Figure to Figure 2.2, it is important to notice that the ideal SCF was calculated as an analytic expression, whereas the COF was estimated for a simulated GFSK signal with noise introduced. The signals contains 5 samples per symbol, the block length is 30.000 samples and the DFT-length is set to 250. Since this Figure is the result of a practical estimation, the (f, α)-parameterization is changed to the (f_1, f_2)-notation, as explained in Section 2.2.

Figure 2.3.: COF Estimation for a simulated GFSK Signal

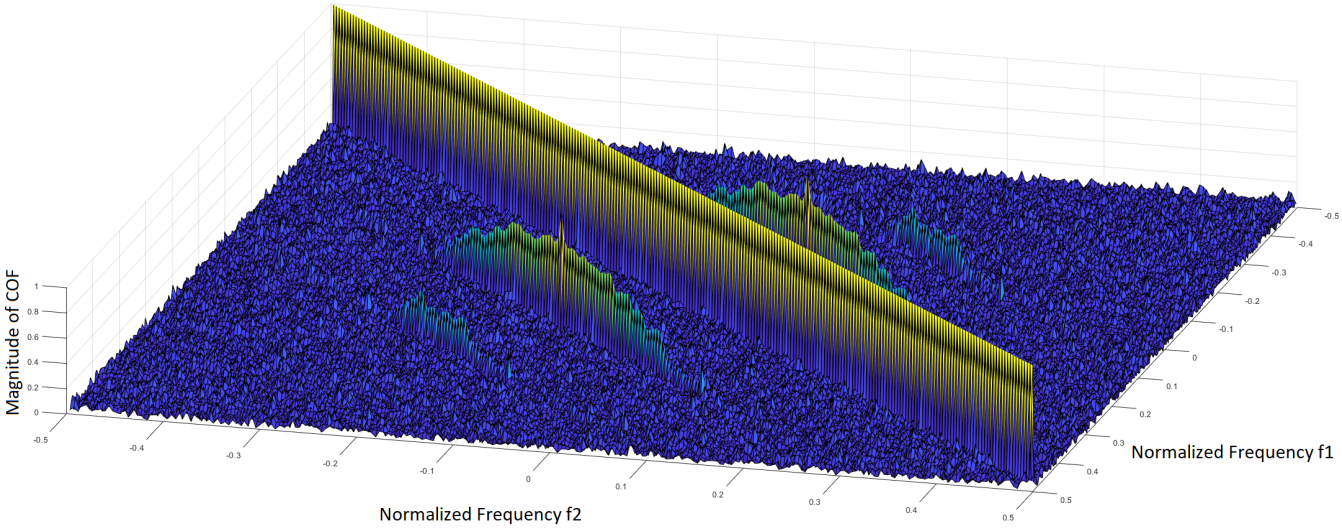

2.1.4. Advantages of Cyclic Spectral Analysis over Conventional Spectral Analysis

This thesis only uses a fraction of the giant field of cyclic spectral analysis. For completeness, it should be mentioned that various other methods exist, like cyclic moments, cyclic cumulants and cyclic polyspectra of higher order, which can also be used for signal detection and parameter estimation. This Section discusses only the benefits relevant for this thesis.

Cyclic spectral analysis is considered to be noise and interference tolerant. It might be impossible to detect the presence of multiple, overlapping signals in a conventional PSD, whereas the SCF provides clearly distinguishable indicators. Since it is highly likely that multiple, overlapping signals consist of different modulations or contain

different symbol rates, their cyclic features will have different shapes and appear at different positions in the SCF. Moreover, in an AWGN channel the PSD is an additive representation of the PSD of WGN and the PSD of a signal. Regardless how long the observation time is, there is always an uncertainty due to the influence on the PSD by noise. In the SCF, this corruption is only present at the α-slice at $\alpha = 0$. All other values of α are uncorrupted, since the behaviour of different frequencies of WGN is uncorrelated as the observation time approaches infinity.

Example: Figure 2.4 shows the estimated PSD of two directly overlapping BPSK signals, both without frequency offsets. Both signals are simulated with a square-root raised cosine pulse shaping with a roll-off factor of $\beta = 0.5$. The two BPSK signals vary only in their symbol rate: One has $f_1 = 4\frac{samples}{symbol}$, while the other one has $f_2 = 6\frac{samples}{symbol}$. By inspecting the PSD, it is difficult to determine, whether one or multiple signals are present.

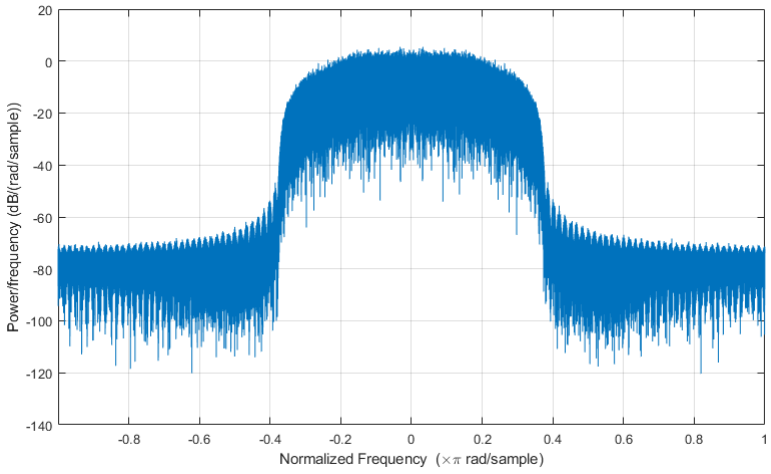

Figure 2.4.: Periodogram Estimation of two directly overlapping BPSK Signals

In comparison, Figure 2.5 shows the estimated SCF for the same sample sequence. While on the diagonal axis yields the PSD, it can be observed that distinct cyclic features, caused by distinct symbol rates, reveal the presence of two signals. The shape of each cyclic feature can be used to classify the modulation type. The (f, α)-parameterization is changed to the (f_1, f_2)-notation, as explained in Section 2.2.

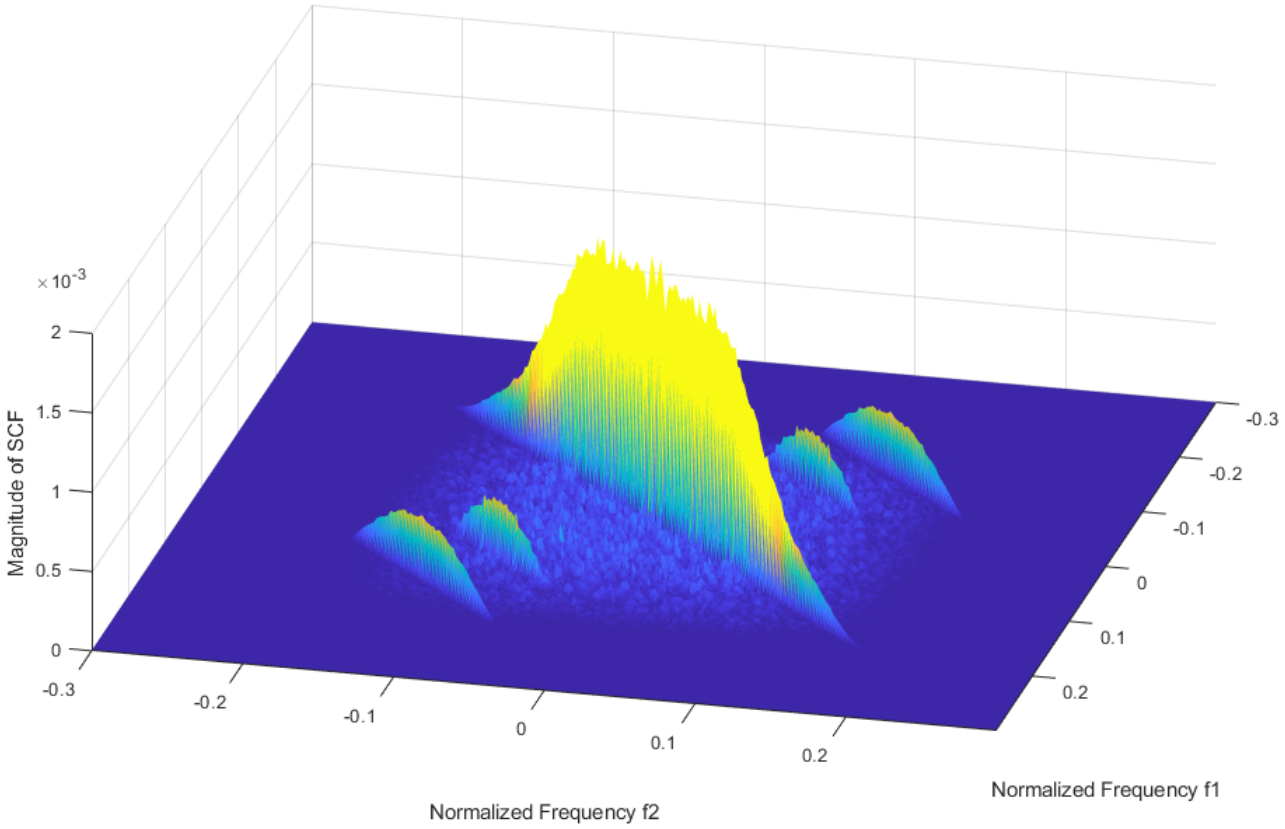

Figure 2.5.: SCF Estimation of two directly overlapping BPSK Signals

The shape of the features in the SCF depend strongly on the type of modulation. By comparing the estimated feature to a known feature, modulation recognition can be performed. A great overview of common communication signals and their highly distinct SCFs can be found in the *Gallery of Spectral Correlation* [1].

Cycle frequencies of a signal are influenced by its parameters. For many modulation types, cyclic features can be found at multiples of the symbol rate and frequency offsets would lead to offsets in the α-slice. Therefore, those parameters can easily be estimated by evaluation of the SCF. Many other practical problems, like system identification, time difference of arrival estimation and many synchronisations tasks, can be encountered by the exploitation of cyclostationarity. Those are not discussed in this thesis and the reader is referred to [7] for a detailed discussion.

2.2. Estimation of Spectral Correlation

The definitions of the previous section include limiting operations, where for example the observation time approaches infinity. Since this thesis copes with practical prob-

lems, it is necessary to introduce at least one method for the measurement of spectral correlation.

2.2.1. Time Smoothing Method

The Time Smoothing Method (TSM) is a consistent estimator for the SCF and consequently for the COF. For proof and a detailed derivation of the method, the reader is referred to [9] and [10]. The TSM can again be explained in strong analogy to a conventional algorithm, namely the Bartlett-method for the estimation of the PSD. Whereas the Bartlett-method computes multiple periodograms and averages eventually to provide consistency, the TSM computes multiple cyclic periodograms and then applies averaging. The algorithm can be summarized in the following steps:

- Divide all samples, collected in the observation time T, in M sub-blocks, each of length N,
- apply a DFT of length N to each sub-block,
- calculate a cyclic periodogram of each DFT output,
- multiply a phase compensation factor to each cyclic periodogram,
- average over all cyclic periodograms to obtain the SCF estimation.

Since the phase compensation factor finds little attention in the literature, an explanation of its importance is given in Appendix C.

The effectiveness of this method can be observed clearly, assuming interference and noise causing frequency components f_k and f_j to have a power of σ_k^2 and σ_j^2. Using conventional spectral analysis, like a radiometer based approach, the detection of PropCube's signal has to cope with the full power σ_k^2 and σ_j^2. In comparison, equation 2.12 defines the cyclic periodogram to be a multiplication of two frequency components, leading to a variance of $\sigma_k \sigma_j$ at the corresponding position, assuming uncorrelatedness of f_k and f_j. Again, it can be noticed that for $\alpha = 0$, i.e. $k = j$, it results in the conventional periodogram with power σ_k^2. Averaging over multiple sub-blocks allows the application of the central-limit-theorem, which leads to a variance reduction by a factor of $\frac{1}{M}$. Therefore, the influence of noise and interference, that does not exhibit particular cycle frequencies, can greatly be decreased, approaching zero for observation times approaching infinity.

For the TSM, the spectral resolution is $\Delta f = \frac{1}{N}$ [9]. Therefore, an increase in the sub-block length N yields a finer resolution, but also causes the estimate to have a greater variance as the observation time stays constant, because the number of sub-blocks M decreases. This relation is derived in [2] and expressed in terms of a coefficient of variation C, defined by

$$C \approx \frac{C_0}{\Delta T \Delta F \mid C_x^{\alpha}(f) \mid^2}, \tag{2.16}$$

where $C^{\alpha}(f)$ is the spectral coherence function introduced in 2.15 and C_0 is a constant in the order of unity. In [2], C_0 is derived in detail, here 2.16 is presented to provide an insight into the interactions of various design parameters. In general, an estimation is said to be statistically reliable, if the time-resolution-product fulfills the following condition:

$$\Delta T \Delta F \gg 1. \tag{2.17}$$

Relations 2.16 and 2.17 point out the trade-offs which must be taken for a practical implementation. High statistical reliability opposes a fine spectral resolution. The length of the observation time T might be limited by practical circumstances, like the Doppler rate in this thesis. Eventually, all of those factors must match under the requirement of computational tractability. For an in-depth discussion of the resolution parameters, the reader is referred to [9] and [2].

The TSM is a straightforward method to estimate the SCF. There exist various alternative algorithms, like the frequency smoothing method, the FFT accumulation method and the strip spectral correlation analyzer to name the most important. Those algorithms are derived in detail in [9].

2.2.2. Implementational Aspects

In the literature of cyclic spectral analysis, the variables α and f are common to represent the frequency separation and the center frequency, as described earlier in Section 2.1.2. However, this raises complications in the practical implementation with discrete frequency bins. Therefore, in the following the parameterization will be changed to a equivalent notation with $f1$ and $f2$ where:

$$f1 = f - \frac{alpha}{2}, \tag{2.18}$$

$$f2 = f + \frac{alpha}{2}. \tag{2.19}$$

In that manner, it is more convenient to compute the SCF as a two dimensional array, where one dimension corresponds to $f1$ and the other one to $f2$.

Additionally, it might seem intuitive to use a power of 2 for the DFT-length N for each subblock in the TSM. However, it is useful to choose the combination of all parameters so that cyclic features, like peaks in the SCF, correspond to an integer tuple $(f1, f2)$ of array indices, so that no leakage across multiple indices occurs. Also, for example for synchronization tasks, it is beneficial if the number of samples per symbol is an integer value. Choosing a DFT-length N other than a power of 2 might be the

easiest way to fulfill these conditions.

Example: The GFSK-signal used for Propcube has a symbol rate of $f_{symb} = 9.6kHz$. If a sampling frequency of $f_{samp} = 48kHz$ is chosen, the number of samples per symbol is $\frac{f_{samp}}{f_{symb}} = 5$. The most important second-order cyclic feature of this signal arises at the cycle frequency $\alpha = f_{symb}$. To avoid leakage, it is therefore useful to choose the DFT-length N so that the α-slice at $\alpha = 9.6kHz$ falls into integer array indices. This is satisfied for example, when N is chosen to be 500: $\frac{f_{symb}}{f_{samp}} \times N = \frac{9.6kHz}{48kHz} \times 500 = 100$. With this value of N, the α-slice can be found at array index tuples $(f1, f2)$ where the condition $|f1 - f2| = 100$ is fulfilled.

2.3. Cycle Detectors

Cycle detectors were originally proposed by Gardner in [11]. The main benefit of cycle detectors is that cyclostationary characteristics of communication signals are exploited. Ideally, estimated cyclic features at all cycle frequencies exhibited by the signal are weighted by the known, true cyclic features. The multi-cycle detector is therefore defined by

$$\gamma = \sum_{\alpha} \int_{-\infty}^{+\infty} \hat{S}_{x_T}^{\alpha}(f)^* S_s^{\alpha}(f) df, \tag{2.20}$$

where $S_s^{\alpha}(f)$ is the ideal SCF of the sent signal $s(t)$. $\hat{S}_{x_T}^{\alpha}(f)$ is the estimated SCF of the received signal $x(t) = s(t)n(t)$ with observation time T. Hence, $n(t)$ represents a noise process. If the detection statistic γ is above a defined threshold, a signal is detected. The multi-cycle detector uses all cycle-frequencies, which is superior to using only a subset. However, for practical implementations, it is necessary to obtain the timing information of the signal, since the phase of cyclic features depend on both, timing and cycle frequency, as expressed by [11]:

$$S_{s'}^{\alpha}(f) = S_s^{\alpha}(f) e^{-i2\pi\alpha t_0}, \tag{2.21}$$

where $s'(t) = s(t - t_0)$ is a time-shifted version of $s(t)$. If t_0 is unknown, it is possible that the superposition of many cyclic features is destructive for the overall detection statistic γ. Since the need of a signal detector arises from the fact that it is unknown, if a signal is present or not, it is unrealistic to assume knowledge about the signal's timing. This destructive behaviour can be avoided by using only one cycle frequency. The resulting detector is called single-cycle detector and defined by

$$\gamma = \int_{-\infty}^{+\infty} \hat{S}_{x_T}^{\alpha}(f)^* S_s^{\alpha}(f) df. \tag{2.22}$$

In many applications, the performance of a single cycle detector is similar to the performance of a multi-cycle detector. This is due to the fact that, like for GFSK, the

magnitude of one cyclic feature is much stronger than the magnitude of all other cyclic features. Considering implementational aspects, a single-cycle detector is far more computationally efficient, since only one α-slice is computed. However, the phase of estimated cyclic features is still unknown due to equation 2.21. Therefore, a practical approach is to use the magnitude of the estimated α-slice and weight it with the magnitude of the ideal α-slice:

$$\gamma = \int_{-\infty}^{+\infty} | \hat{S}_{x_T}^{\alpha}(f)^* \| S_s^{\alpha}(f) | \, df, \tag{2.23}$$

which can be considered to be a *sub-optimal* single-cycle detector.

3. SCF Approximation of a GFSK Signal with h = 1

Napolitano and Spooner [4] derive approximations for the SCF of CPM signals. By expressing a CPM signal with its Laurent representation, closed form expressions for cyclic features can be given. The results of this work are used in this chapter to derive the SCF for a special case of CPM, namely PropCube's GFSK signal. It will be shown in Section 3.2 that the expressions for SCFs of a GFSK signals can only be evaluated numerically. Figures of the relevant steps and the final results are provided.

3.1. Analytical Expression

Section *C* in [4] is dedicated to *Cyclic Parameters for Integer Modulation Index*, which applies to Propcube's GFSK with modulation index h = 1. First, it is shown in (47) that, for an integer modulation index, the CPM signal contains tones. In this case, the signal can be decomposed as in equation (48):

$$s_{CPM}(t) = E^{\{\alpha\}}\{s_{CPM}(t)\} + z(t) \tag{3.1}$$

where $E^{\{\alpha\}}$ is the periodic-component extraction operation and therefore contains the periodic component of $s_{CPM}(t)$, whereas $z(t)$ is defined to contain the non-periodic component. In general, the SCF is a special case of cyclic polyspectra of order two [2]. For those it holds that the SCF of the periodic and non-periodic components are additive. This can be exploited to achieve the SCF for the entire CPM signal:

$$S^{\alpha}_{\mathbf{CPM}}(f) = S^{\alpha}_{E^{\{\alpha\}}\{s_{CPM}(t)\}}(f) + S^{\alpha}_{\mathbf{z}}(f). \tag{3.2}$$

Most cyclic parameters only depend on $z(t)$, therefore the periodic term is not taken into consideration in the further derivation in the original paper. Eventually, in (58) the equation for second-order cyclic polyspectra for the non-periodic component $z(t)$ is presented as

$$S^{\alpha}_{\mathbf{z}}(f) = i^{\mathbf{1}^{(-)r}\mathbf{1}} \frac{1}{T} \overline{B}^{\alpha}_{1}(f) \tilde{U}^{\alpha}_{\mathbf{a}}(\nu') \Big|_{\tilde{\alpha}=\alpha T, \nu = fT} \quad , \tag{3.3}$$

The term $\mathbf{1}^{(-)r}\mathbf{1}$ describes the conjugation configuration of the polyspectrum. In the non-conjugate case, which is used throughout this thesis, it can be simplified further to

$$S^{\alpha}_{\mathbf{z}}(f) = \frac{1}{T} \overline{B}^{\alpha}_{1}(f) \tilde{U}^{\alpha}_{\mathbf{a}}(\nu) \Big|_{\tilde{\alpha}=\alpha T, \nu = fT} \quad , \tag{3.4}$$

where

$$\tilde{U}_{\mathbf{a}}^{\alpha}(\nu) = \sum_{m\in\mathbb{Z}} (-1)^m \tilde{R}_{\mathbf{a}}^{\tilde{\alpha}}(m) e^{-j2\pi\nu m} \tag{3.5}$$

and

$$\overline{B}_1^{\alpha}(f) = \overline{Q}_1(\frac{\alpha}{2} - f)\overline{Q}_1(\frac{\alpha}{2} + f). \tag{3.6}$$

It can be observed that $S_{\mathbf{z}}^{\alpha}(f)$ depends on two factors: The CACF of the data symbols $\tilde{R}_{\mathbf{a}}^{\tilde{\alpha}}(m)$ and the Fourier transform of the real-valued pulse $\overline{q}_1(t)$, which is expressed by $\overline{Q_1}(f)$ and derived from the Laurent representation of the CPM signal. Equation 3.6 is modified in this thesis to the symmetric version of (60) in [4]. In the original paper, an asymmetric representation is chosen, since it is more convenient to use for orders higher than 2. However, in this application a symmetric representation fits best.

As mentioned in the previous paragraph, $\tilde{U}_{\mathbf{a}}^{\alpha}(\nu)$ in 3.5 is influenced by the CACF of the data symbols in the modulation sequence. Since those are assumed to be independent and identically distributed due to scrambling applied in PropCube, 3.5 simplifies greatly. The CACF can then be expressed as

$$\tilde{R}_{\mathbf{a}}^{\tilde{\alpha}}(m) = \begin{cases} \delta(m), & \text{if } \alpha = 0 \mod (\frac{1}{T}) \\ 0, & \text{other,} \end{cases} \tag{3.7}$$

where $\delta(m)$ is Kronecker's Delta. Consequently, 3.5 is simply expressed by

$$\tilde{U}_{\mathbf{a}}^{\alpha}(\nu) = \begin{cases} 1, & \text{if } \alpha = \frac{k}{T}; k \in \mathbb{Z} \\ 0, & \text{other.} \end{cases} \tag{3.8}$$

The SCF of the non-periodic component $S_{\mathbf{z}}^{\alpha}(f)$ can therefore be expressed as

$$S_{\mathbf{z}}^{\alpha}(f) = \begin{cases} \frac{1}{T}\overline{Q}_1(\frac{\alpha}{2} - f)\overline{Q}_1(\frac{\alpha}{2} + f), & \text{if } \alpha = \frac{k}{T}; k \in \mathbb{Z} \\ 0, & \text{other.} \end{cases} \tag{3.9}$$

In order to obtain $S_{\mathbf{CPM}}^{\alpha}(f)$, also the SCF of the periodic component $S_{E^{\{\alpha\}}\{s_{CPM}(t)\}}^{\alpha}(f)$ must be calculated. This is considered to be trivial, once the periodicities are known. In [4] it is shown in equation (48) that for $h = 1$, the periodic component can be expressed by

$$E^{\{\alpha\}}\{s_{CPM}(t)\} = c_{\infty} \sum_{k=-\infty}^{+\infty} (-1)^k \overline{q}_{\mathbf{0}}(t - kT), \tag{3.10}$$

where c_{∞} is a either +1 or −1 and $\overline{q}_{\mathbf{0}}(t - kT)$ is, for a second-order cyclic polyspectrum, defined by

$$\overline{q}_0(t) = cos[\varphi(t)]rect\left(\frac{t - T/2}{T}\right), \tag{3.11}$$

where $\varphi(t)$ is known as the phase response to the pulse $g(t)$ used in the CPM modulation. By inserting this function, which will later be introduced in 3.15, into 3.11, it results that the period contained in 3.10 is $2T$ and therefore tones at the frequencies $+\frac{1}{2T}$ and$-\frac{1}{2T}$ are present. This might seem intuitive, since a modulation index of $h = 1$ implies a frequency separation by $\frac{1}{T}$. It follows that $S^{\alpha}_{E\{\alpha\}\{s_{CPM}(t)\}}(f)$ is defined by

$$S^{\alpha}_{E\{\alpha\}\{s_{CPM}(t)\}}(f) = \begin{cases} \delta(f - \frac{1}{2T}) + \delta(f + \frac{1}{2T}), & \text{if } \alpha = 0 \\ \delta(f), & \text{if } \alpha = \frac{1}{T} \\ 0 & \text{other.} \end{cases} \tag{3.12}$$

By adding the periodic component 3.12 and non-periodic component 3.9 according to equation 3.2, it eventually follows for the SCF as final result:

$$S^{\alpha}_{s_{\mathbf{CPM}}}(f) = \begin{cases} \delta(f - \frac{1}{2T}) + \delta(f + \frac{1}{2T}) + \frac{1}{T}\overline{Q}_1(f)^2, & \text{if } \alpha = 0 \\ \delta(f) + \frac{1}{T}\overline{Q}_1(\frac{1}{2T} - f)\overline{Q}_1(\frac{1}{2T} + f), & \text{if } \alpha = \frac{1}{T} \\ \frac{1}{T}\overline{Q}_1(\frac{\alpha}{2} - f)\overline{Q}_1(\frac{\alpha}{2} + f) & \text{if } \alpha = \frac{k}{T};\ k \in \mathbb{Z} \text{ and } k \neq 1 \\ 0 & \text{other.} \end{cases} \tag{3.13}$$

3.2. Numerical Evaluation

The real-valued pulse, which is used in 3.6, is defined for a full response system by

$$\overline{q_1}(t) = sin[\varphi(t)]rect\left(\frac{t - T/2}{T}\right), \tag{3.14}$$

where

$$\varphi(t) = \int_0^t g(u)du \tag{3.15}$$

is known as phase response to the pulse used in the CPM signal. Full response refers to the fact that $\varphi(t) = h\pi$ for $t \geq T$.Due to the Laurent representation, PropCube's GFSK signal is approximated as a full-response system. In general, for $h = 1$, $g(t)$ is a Gaussian pulse defined by

$$g(t) = \frac{\pi}{2T}\left[erfc\left(\frac{t/T - 1/2}{\tilde{\delta}\sqrt{2}}\right) - erfc\left(\frac{t/T + 1/2}{\tilde{\delta}\sqrt{2}}\right)\right], \tag{3.16}$$

where

$$\tilde{\delta} = \frac{\sqrt{\ln 2}}{2\pi BT}. \tag{3.17}$$

Since it is impossible to determine an analytical expression for the integral over a Gaussian function, 3.15, 3.14, 3.6 and eventually the SCF have to be determined numerically. The following Figures illustrate the steps to calculate $Q_1(f)$ for $T = \frac{1}{9600}s$, $BT = 0.5$ and $h = 1$:

Figure 3.1.: Gaussian pulse g(t) windowed in time domain to be full-response system

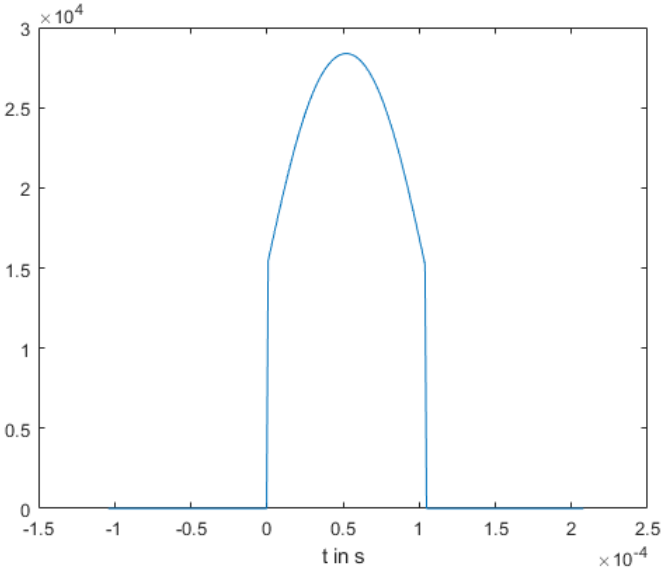

Figure 3.2.: $\phi(t)$ is Phase response function

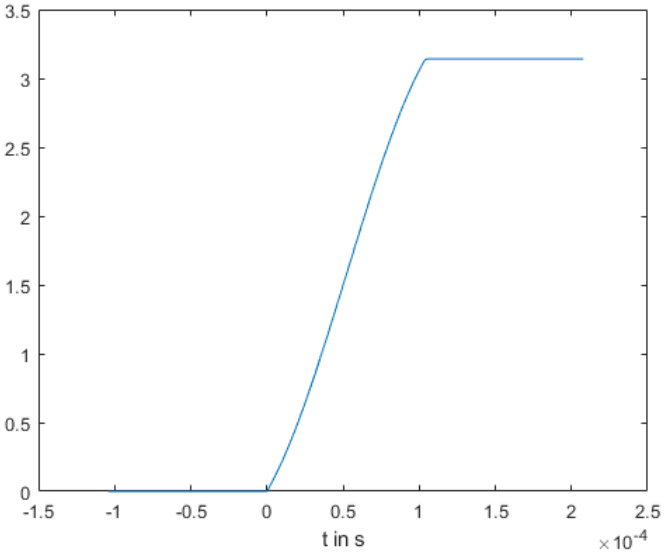

Figure 3.3.: $\overline{q_1}(t)$ is Laurent pulse approximation

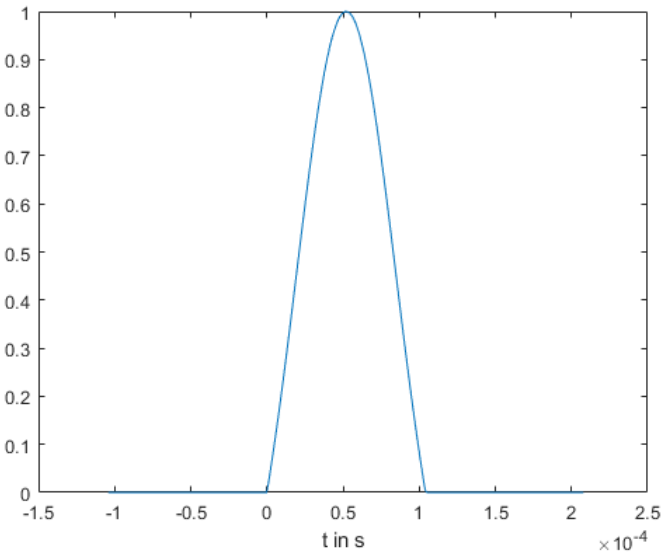

Figure 3.4.: $\overline{Q_1}(f)$ is Fourier transform of $\overline{q_1}(t)$

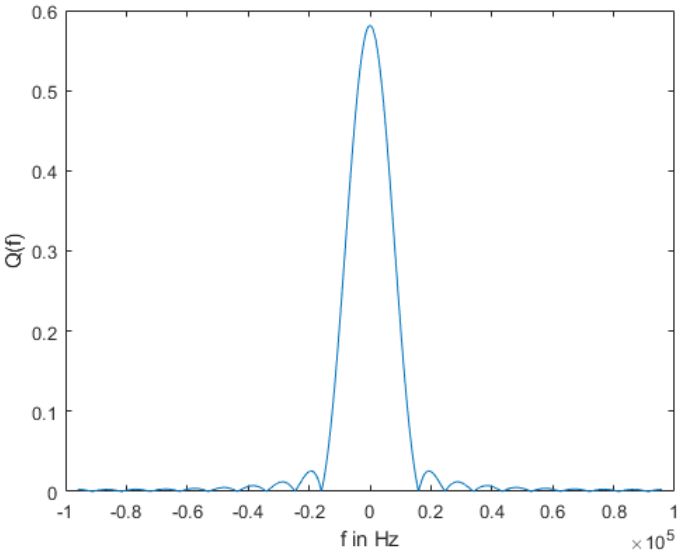

The final result for the SCF is depicted in Figure 2.2. It is important to notice that the sharp peaks pictured with height 1 are ideally of infinite height.

4. Detector Design

In this chapter, the design of the proposed signal detection algorithm is developed. First, the current communication environment is explained and requirements for the detector are determined. This thesis is meant to provide a general solution for signal detection under high Doppler rate and high interference. Nevertheless, it is motivated by the practical application in the SSAG's CubeSat program. Step by step, the detection algorithm is built in the following sections. The most important part of the final algorithm is the detection statistic, its development is the core achievement of this thesis. While Section 4.2.1 discusses the benefits of SCF- and COF-based statistics, Section 4.2.2 is determined to evaluate various SCF-based approaches before the development of an adaptive detection statistic is motivated. As briefly mentioned in Chapter 1, the influence of the Doppler rate complicates the measurement of cyclic features. To be able to cope with that, this thesis introduces design parameters which limit the amount of possible smearing by exploitation of a finite DFT resolution and a known upper bound for the Doppler rate. At this point, where it is possible to estimate the α-slice and to apply a detection statistic, an algorithm is proposed in Section 4.4.1, which performs on an incoming stream of sampling data. Since the detection statistic provides not only information about the presence of a signal, but also the instantaneous Doppler shift, a method, which takes multiple detection points into account to correct time-varying frequency offsets, is developed in Section 4.4.2.

Signal detection is often described as a hypothesis-testing problem. Depending on a detection statistic, the detector yields hypothesis H_0 or H_1, defined as

$$\begin{aligned} H_0: &\quad y(t) = w(t), \\ H_1: &\quad y(t) = s(t) + w(t), \end{aligned} \tag{4.1}$$

where $y(t)$ is the received signal, $s(t)$ is the signal to be detected and $w(t)$ represents WGN. While this model may be adequate for many applications, it obviously fails to hold for signal detection in the ISM band. The more challenging hypothesis testing problem can be formulated as

$$\begin{aligned} H_0: &\quad y(t) = i(t) + w(t), \\ H_1: &\quad y(t) = s(t) + i(t) + w(t), \end{aligned} \tag{4.2}$$

where $i(t)$ is interference with arbitrary characteristics like signal strength, center frequency, modulation scheme, pulse-shaping and data rate, to name the most important.

Methods, which work reliably for example for problems as 4.1, might not be applicable to problem 4.2 since they could raise false alarms, when an interferer exceeds an energy threshold. As discussed in the course of this thesis, cycle detectors are a promising approach for signal detection in problems similar to problem 4.2. Nevertheless, problem 4.1 can be used as a performance benchmark as presented in Section 5.1.

Again, it is to be mentioned that this thesis does not focus on the derivation of a maximum-likelihood based detection statistic, since this would be only possible for problems posed similar to 4.1. Rather, this thesis focuses on the development of a detection statistic that performs reliably in the ISM environment, as posed in problem 4.2.

4.1. Current Communication System

PropCube satellites are operated by ground stations via a communication uplink not further described in this thesis. To be able to react on information received from the satellite, the signal detector must be able to perform close to real time. If this restriction would not apply, the detector could use all data of one overflight and perform signal detection and frequency correction as post processing. In such a manner, the reliability of the algorithm's output could be increased. False alarms could easily be marked as an outlier and the interpolation of all detection points would yield a frequency correction curve very close to the true S-curve caused by Doppler rate. This approach was tested in the course of the development of the final detector, but no practical difference was noted, since the amount of false alarms was negligible. In fact, for the final parameter settings no false alarms occurred. Moreover, the deviation of a linear interpolation of detection points for frequency correction, as proposed in Section 4.4.2, to the true S-curve lies below the DFT's resolution and is assumed to be managable for a demodulator in the next processing step.

As described in Section 3, PropCube satellites use a GFSK modulation with a symbol rate of $9600\frac{\text{symbols}}{\text{second}}$ and a modulation index of $h = 1$. The carrier frequency is set to $914MHz$. The data is transmitted according to an amateur radio protocol known as AX.25. One burst is composed of a 400 byte synchronization preamble and 3 AX.25 packages. Each AX.25 package begins with a one byte start flag, followed by a 16 byte header and a data frame. Eventually, a CRC code is appended before a stop byte terminates the package. Since the start and stop bytes are not allowed to be used anywhere else in the package, bit stuffing is applied, which results in a variable package length. The NRZI encoded package is scrambled before the data is finally transmitted. After each burst, which lasts usually for around 1 second, a break of 3 to 10 seconds leads to an overall duty cycle below 25% during one overflight. Figure 4.1 shows the spectrogram of a typical PropCube signal with low interference. It can be seen that the Doppler shift occurring in 15 seconds causes a frequency deviation in the order of a few kHz.

Figure 4.1.: Spectrogram of a typical PropCube Signal

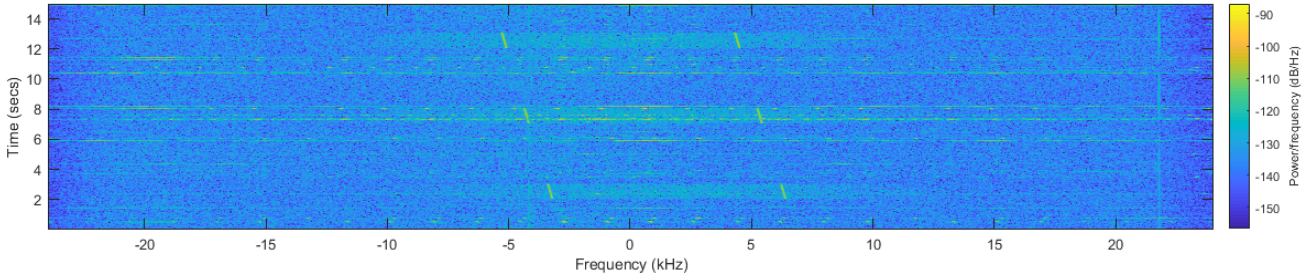

4.2. Design Considerations

4.2.1. Comparison of SCF or COF based Detection Statistic

Often it is beneficial to use a detection statistic based on the COF, since it can cope with changes in the SNR better than the SCF. This would be the case, if only the transmit power varies due to the movement relative to the ground station and the detection problem was posed in a WGN-only environment, as defined in 4.1. However, problems arise due to interference, for which the time-resolution-product condition $\Delta T \Delta F \gg 1$ is not fulfilled. Such an interferer only appears for a short time and has therefore a highly erratic SCF α-slice estimation. Calculating the COF might upscale the contribution of interference since its energy could be very low due to its short presence. Hence, the erraticity is amplified.

Example: Figure 4.2 shows the spectrogram of a 200ms *segment of a PropCube burst, sampled at* 48kHz*. The lower and the upper tone of the GFSK modulation are clearly visible at* $-2.4kHz$ *and* $7.2kHz$ *as thin, continuous lines, resulting in a center frequency of* 2.4 kHz*.*

Figure 4.2.: Spectrogram of a burst part with a moderate interferer

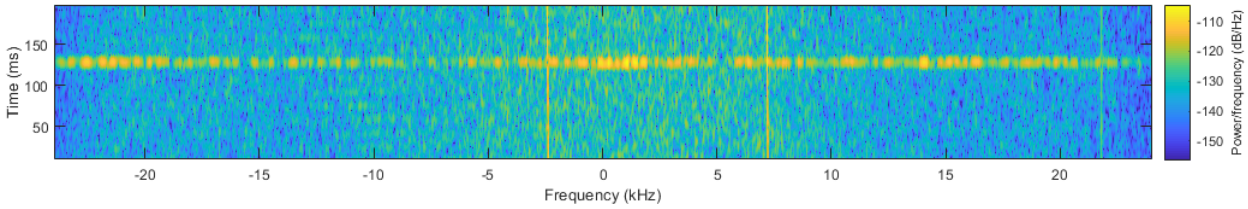

The corresponding COF estimated with the TSM for a cycle frequency of $\alpha = 9.6kHz$ *and a DFT length of* $N = 500$ *is shown in Figure 4.3. The interferer, that occurs around* $t = 130ms$ *only appears for a fraction of the overall observation time, which leads to a highly erratic COF estimation. In comparison, the estimated SCF at* $\alpha = 9.6kHz$ *for the same sample sequence is depicted in Figure 4.4.*

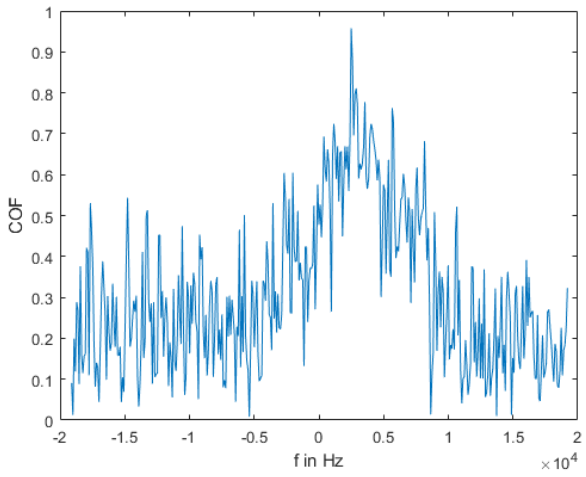

Figure 4.3.: Estimated COF

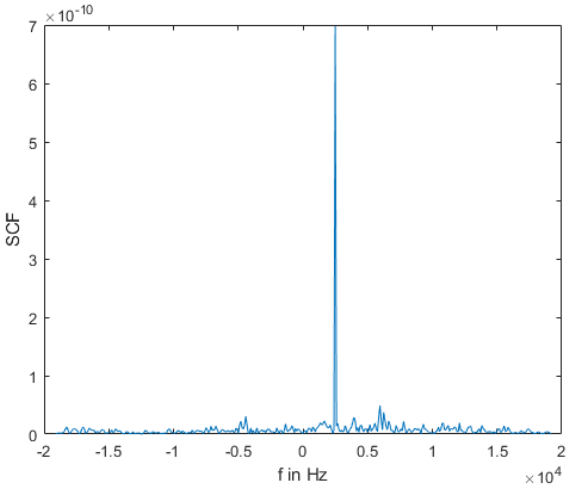

Figure 4.4.: Estimated SCF

To avoid the amplification of erraticity in the cyclic feature estimation of short, low-energy interference, it is beneficial to use a SCF-based detection statistic. To cope with the power dependency of the SCF, an adaptive approach is developed in Section 4.2.2.

4.2.2. Adaptive Detection Statistic

When implementing a single-cycle detector, as described in Section 2.3, the detection statistic γ is calculated by evaluation of

$$\gamma = \int_{-\infty}^{+\infty} | \hat{S}^{\alpha}_{x_T}(f)^* \| S^{\alpha}_s(f) | \, df, \tag{4.3}$$

where T is the block length and $S^{\alpha}_s(f)$ is the ideal SCF, which can be interpreted as a weighting function. Due to the derivation of the ideal SCF of PropCube's GFSK signal in Chapter 3, it is known that the ideal α-slice for the strongest cyclic feature at $\alpha = \pm 9.6kHz$ can be expressed by

$$S^{9.6kHz}_{S_{\text{CPM}}}(f) = \delta(f) + \frac{1}{T_s}\overline{Q}_1(\frac{1}{2T_s} - f)\overline{Q}_1(\frac{1}{2T_s} + f), \tag{4.4}$$

where T_s is the symbol period. The theoretical infinite height of the Dirac delta $\delta(f)$ is limited by the resolution of the Fourier-transform and scaled by the signal power. The shape of the ideal α-slice is depicted in Figure 4.5 in comparison to the estimated α-slice of a simulated GFSK signal.

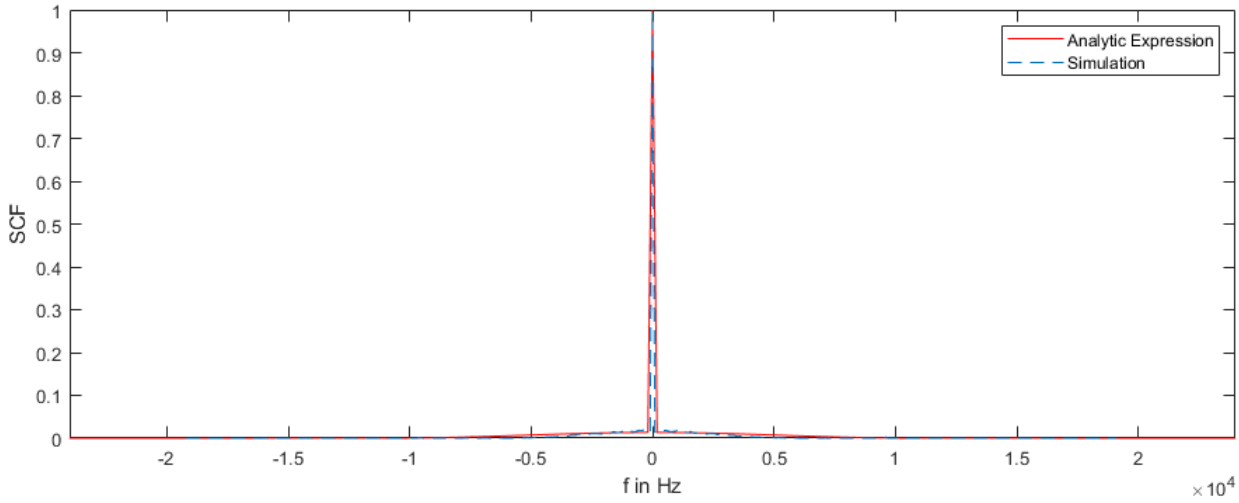

Figure 4.5.: Analytic α-slice compared to a Simulation, both normalized to unity at $\alpha = 9.6kHz$

It is easy to see that the peak has a sharp, striking form whereas the lobe-like component is close to zero. Using this shape as a weighting function under interference leads to false alarms, since it only weights the amount of spectral correlation in the α-slice. Assuming there is an interferer, which exhibits a cyclic feature at $\alpha = 9.6kHz$ of sufficient magnitude, the threshold might still be exceeded after application of the weighting function. In other words, the cycle-detector fails to put hard restrains on the shape of the α-slice. Moreover, the imbalance of signal power between interferers and PropCube's signal additionally mitigates the effectiveness of a weighting function. In Figure 4.6, this issue is addressed: A strong BPSK interferer with a symbol-rate of $9.6kHz$ causes a strong lobe-like cyclic feature in the α-slice, illustrated in blue. Every shift of the weighting function in between the two illustrated positions would lead to a detection statistic γ that exceeds the threshold.

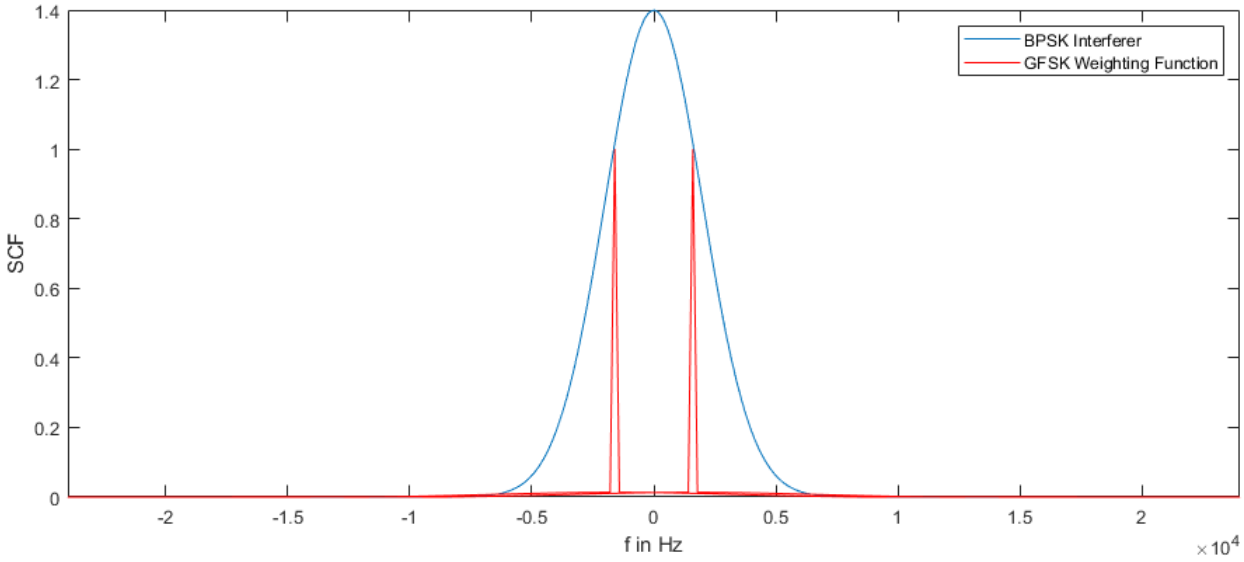

Figure 4.6.: Two possible positions of the GFSK weighting function, which would raise false alarms when an interferer like the illustrated BPSK signal is present

Although the presence of an interferer like in Figure 4.6 is unlikely, it demonstrates the susceptibility of the weighting function to raise false alarms for any kind of interference-caused contribution in the α-slice. This matter is complicated by a limited observation time: If the observation time could approach infinity and no Doppler rate would cause a continuous frequency shift, the shape of the analytically derived α-slice would be identical to the estimated α-slice in a WGN environment, neglecting minor distortions resulting from a finite spectral resolution Δf. However, a limited observation time introduces noise in the α-slice, which leads to an erratic shape. For short observation times, the lobe-like component seems to be indistinguishable from this noise. Hereby is the significance of the weighting function drastically reduced, since it relies on the presence of the peak only. Hence, it is reasonable to develop a modification of the standard single-cycle detector when an operation under interference is desired.

Another approach to define a detection statistic could by via a metric. Instead of weighting the estimated α-slice with the ideal one, a distance between both can be calculated. If the distance is below a certain threshold, the detector yields a detection. While this might be a promising approach for other types of modulation, like BPSK where the cyclic feature consists only of one strong and wide lobe-like component, it is again prone to raise false alarms for PropCube's GFSK signal in the ISM environment. Due to the fact that the estimated α-slice differs from the ideal α-slice by noise, a standard distance is introduced. In combination with a high variance, a metric was tested to be a less significant detection statistic. This method could be improved by first estimating the WGN power and then defining the ideal α-slice under consideration of the noise-floor. It was not pursued further, since the WGN estimation in the ISM band

leads to great complications and exceeds the tractability in this thesis.

Both methods, weighting with the ideal α-slice and distance calculation to the ideal α-slice, are required to be combined with an exhaustive search since the position of the signal in the frequency domain is unknown due to the Doppler shift. The detection statistic must therefore be computed for every possible frequency shift of the α-slice.

Clearly, the sharp peak in the α-slice is the most promising detection feature. Based on that, the approach proposed in this thesis is an adaptive peak detection. The maximum magnitude of the α-slice is determined and all other values are checked to be below a certain threshold relative to the peak height. Therefore, this method can be interpreted as drawing an upper bound for the expected α-slice, which is scaled by its maximum. If no point violates the upper bound condition, the detector yields a detection and the position of the maximum height reveals the Doppler shift. Hence, it is not required to compute a distance or statistic for every possible frequency shift of the α-slice. The trade-off taken here is the following: If a cyclic feature exists at $\alpha = 9.6kHz$ and the shape differs significantly from a single peak, the measurement is discarded even if PropCube's GFSK signal is also present. The metric- or weighting-based approaches would indeed raise a detection, but are very likely to also raise a false alarm in the absence of PropCube's GFSK signal. Significance of a peak is defined as a design parameter in terms of the adaptive threshold parameter κ. Consequently, it can be claimed that this method reduces the false alarm rate on the expense of false negatives. However, since the observation time for one TSM estimation is much smaller than the duration of one burst and those observation times are chosen with an overlap, it is highly unlikely that an entire burst is missed because of interference at the same cycle frequency. The threshold value κ defines the threshold T_{AS} by

$$T_{AS}(f) = \kappa \times H_{max} + \iota(f) \times H_{max}, \tag{4.5}$$

where H_{max} is the maximum value in the estimated α-slice and $\iota(f)$ is the lobe-like component of the ideal α-slice. Multiplication of $\iota(f)$ with H_{max} scales the lobe-like component according to the signal power. Due to residual smearing, this threshold is then applied to all points in the α-slice besides the peaks and its neighbors. If a detection is made, the instantaneous Doppler shift is simply revealed by the position of the maximum value in the α-slice.

Example: Figure 4.7 demonstrates the threshold $T_{AS}(f)$ for the ideal α-slice without frequency-offset. In comparison, Figure 4.8 demonstrates the threshold $T_{AS}(f)$ for the α-slice shown in Figure 4.4, corresponding to real-world data presented in Figure 4.2. The maximum in the α-slice is detected at $f_0 = 2496Hz$, which represents the Doppler shift. The threshold $T_{AS}(f)$ can therefore easily be centered around it. Both Figures use $\kappa = 0.12$.

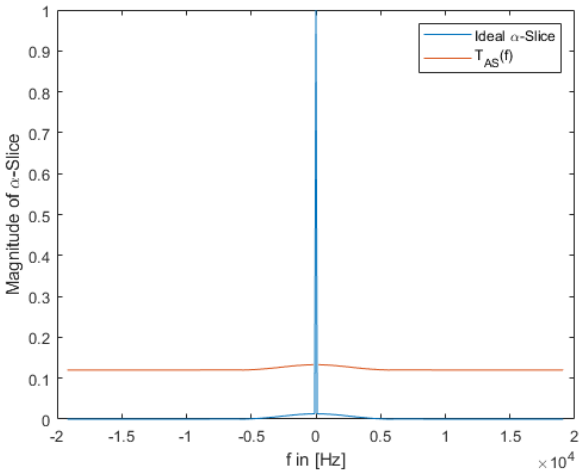

Figure 4.7.: Threshold applied to Ideal α-Slice

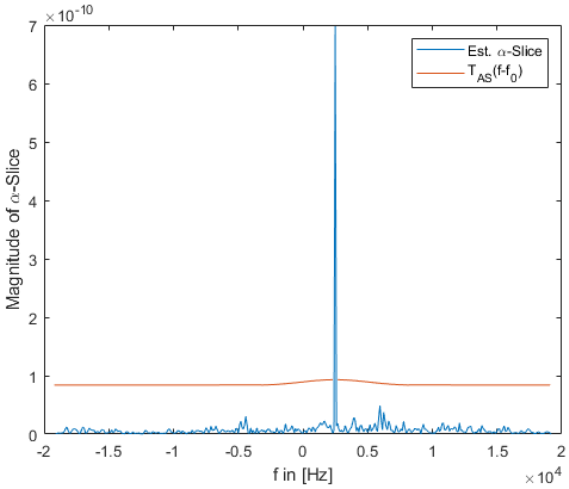

Figure 4.8.: Threshold applied to Real-World Data

4.2.3. Choice of Block Length due to Doppler rate

The expression *observation time*, denoted as T, is closely related to *block length*, represented by the letter B: While the former is usually given in in seconds, the latter is given in units of samples.

In Section 2.1.2, it is explained that the SCF can be interpreted as a correlation of frequency components over time. The Doppler rate causes a frequency shift Δf_{DR} of the signal within time Δt_{DR}. Fig 4.9 illustrates the effect of a constant Doppler rate of $\frac{\Delta f_{DR}}{\Delta t_{DR}} = 8\frac{kHz}{s}$ on two tones similar to PropCube's GFSK signal. Consequently, the correlation of frequency components smears and the estimation of cyclostationary features is complicated. In practice, the measurement of the Doppler rate is limited by the DFT's resolution. For a short observation time and a sufficiently low DFT resolution, the signal seems to have a constant center frequency, since the Doppler rate causes frequency deviations mainly within the same DFT bin. For the sake of a clear demonstration, a DFT length as low as 20 bins was chosen in Figure 4.10. Therefore, the finite resolution of the DFT and a limited observation time can be exploited to apply cyclostationary concepts to signals corrupted by continuous frequency changes.

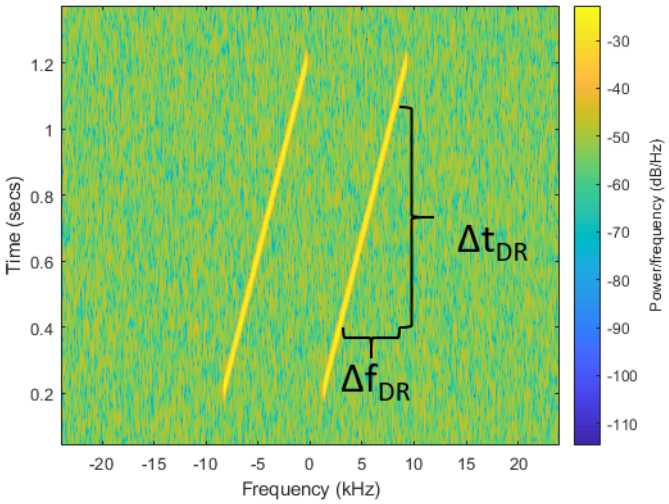

Figure 4.9.: Effect of Doppler Rate $8\frac{kHz}{s}$

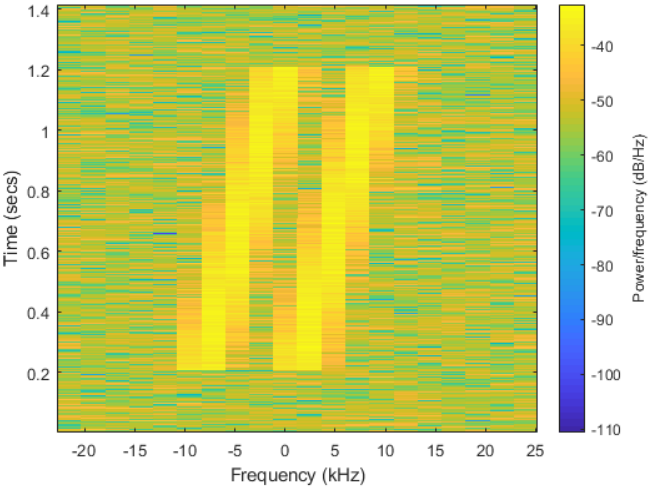

Figure 4.10.: Doppler Rate at low DFT Resolution

By analysis of the orbital mechanics, the maximum value of the Doppler rate δ_{DR} can be determined. Using the simulation capabilities of the *Systems Toolkit (STK)* Software, $\delta_{DR} = 310\frac{Hz}{s}$ was estimated to be a solid upper bound for LEO satellites transmitting at $914MHz$.

A design parameter ϵ is introduced, which limits the block length B for a given DFT resolution under the condition that the maximum possible Doppler shift over one block must be less than ϵ DFT bins. Consequently, the block length B can be determined by evaluation of

$$B = \epsilon \times \frac{f_{samp}}{N} \times \frac{1}{\delta_{DR}} \times f_{samp}, \tag{4.6}$$

where $\frac{f_{samp}}{N}$ is the resolution of a DFT of length N applied to a signal sampled with sampling frequency f_{samp}. Therefore, $\epsilon \times \frac{f_{samp}}{N}$ can be interpreted as the allowed frequency shift in units of DFT bins. Division by δ_{DR} yields the minimum time needed for such a frequency change, multiplication by f_{samp} eventually gives the maximum number of samples, which may be included in one block length.

By empirical studies, a suitable value for ϵ was determined to be $\epsilon = 0.5$. While this value limits the smearing of cyclic features, it can not prevent it completely. It occurs, that one frequency bin is crossed, which leads to two neighboring peaks in the α-slice. However, the minimum possible peak height is at least $1-\epsilon = 0.5$ times the height compared to a case without smearing, which is shown in Chapter 5 to perform sufficiently. The following example illustrates the influence of the block length parameter ϵ.

Example: Using $\epsilon = 0.5$ in addition to the values used for Figure 4.10, i.e. a Doppler rate of $8\frac{kHz}{s}$ and a DFT length as low as 20 bins, yields a block length of $B = 7200$ samples, which corresponds to a observation time of $150ms$ at a sampling frequency of $f_{samp} = 48kHz$. The interval between the two red lines in Figure 4.11 mark the bounds of the resulting block length B, centered at an arbitrary position within the burst.

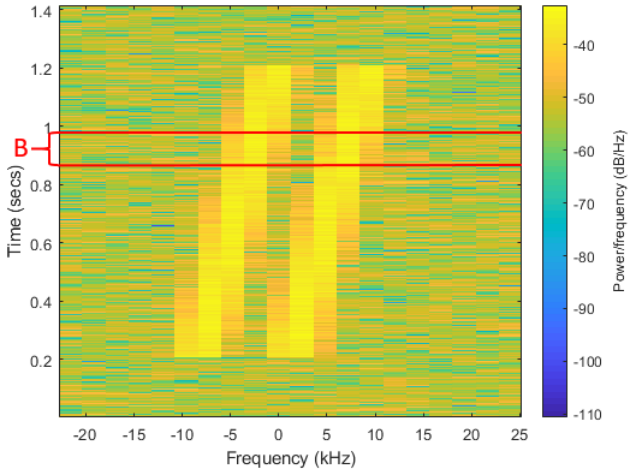

Figure 4.11.: Block Length B for $\epsilon = 0.5$

4.3. Statistics at the TSM Estimator's Output if a white Gaussian Process is applied

Via a step-by-step analysis of the statistics at every stage of the TSM estimator, the distribution at its output can be derived. In that way, it can be seen easily how the choice of design parameters influences the α-slice and how the power of interferers is mitigated.

Assuming that all samples in the observation time solely belong to one Gaussian process with variance σ_n^2, which can be seen as WGN or interference, the time-domain variance is

$$\sigma_{TR}^2 = \sigma_{TI}^2 = \frac{\sigma_n^2}{2} \tag{4.7}$$

in the real and imaginary part of each sample. It is well known that the statistics after applying a DFT, which is defined by

$$X(k) = \frac{1}{N} \sum_{n=0}^{N-1} x(n) e^{-i2\pi k \frac{n}{N}}, \tag{4.8}$$

to only the real time-domain data is also Gaussian with zero mean and a variance $\frac{\sigma_n^2}{4N}$ in both real and imaginary parts. Applying the DFT to both, real and imaginary time-domain data, yields a frequency-domain variance of

$$\sigma_{FR}^2 = \sigma_{FI}^2 = \frac{\sigma_n^2}{2N} \tag{4.9}$$

in real and imaginary parts. In Appendix D it is shown that two frequency components of WGN $X(k_i)$ and $X(k_j)$ are uncorrelated for $i \neq j$. Therefore, the variance of $Y(k_l) = X(k_i)X(k_j)$ is simply

$$\mathrm{var}\{X(k_i)X(k_j)\} = E\{(X(k_i)X(k_j))^2\} = E\{X(k_i)^2)E(X(k_j)^2\} = \mathrm{var}\{X(k_i)\}\mathrm{var}\{X(k_j)\}, \tag{4.10}$$

but the statistics of Y does not follow a Gaussian distribution anymore. Instead, the probability density function can be described by a modified Bessel function of second kind [12]. However, equation 4.10 can be exploited in the next processing step: Cyclic periodograms are calculated by the multiplication of two points of the DFT's output. The variance of a cyclic periodogram for $\alpha \neq 0$ is

$$\sigma_{CR}^2 = \sigma_{CI}^2 = 2\left(\frac{\sigma_n^2}{2N}\right)^2 \tag{4.11}$$

in real and imaginary parts. The various cyclic periodograms are uncorrelated, since they are computed from non-overlapping sub-blocks. Averaging over M sub-blocks allows the application of the central limit theorem, assuming $M \gg 1$, which results again in a zero mean Gaussian distribution and a variance of

$$\sigma_{AR}^2 = \sigma_{AI}^2 = \frac{1}{M}2\left(\frac{\sigma_n^2}{2N}\right)^2 \tag{4.12}$$

in real and imaginary parts. Eventually, the statistics of the magnitude of such a complex variable can be described by a Rayleigh distribution [13] with mean

$$\mu_M = \sqrt{\frac{\pi}{M}}\frac{\sigma_n^2}{2N} \tag{4.13}$$

and variance

$$\sigma_M^2 = \left(1 - \frac{\pi}{4}\right)\frac{1}{M}\left(\frac{\sigma_n^2}{N}\right)^2. \tag{4.14}$$

Now it can easily be seen how the choice of the observation time, which directly influences the number of sub-blocks M and the DFT length N, effects mean and variance of the noise floor. In the discussion of advantages of cyclic spectral analysis in Section 2.1.4, the tolerance against interference is highlighted: While a conventional detector has to cope with the full power of interferers, their power is reduced by an factor of $\frac{1}{M}$

in the α-slice.

Gardner [2] introduces a SNR-relationship for signal detectors: A detector is described to generate a *signal decision* under H_1 or a *noise decision* under H_0, given by the detection statistic γ in either case. It is desirable to have a high SNR, which can be interpreted as a significantly differing detection statistic γ under H_0 and H_1. It is shown that the standard radiometer maximizes this SNR in a stationary WGN environment. This follows the intuition: For example, if a sine-wave is to be detected in WGN, there is no better approach than a conventional Fourier transform, which corresponds to an energy detection in frequency domain. However, in [2] it is also derived that cycle-detectors outperform the radiometer when the signal power varies or interference is present, which is often applicable to real-world problems as posed in this thesis. In practice, a trade-off between a high-resolution $\Delta F = \frac{1}{N}$ and a sufficiently large value of M, which guarantees statistical reliability, must be chosen.

4.4. The Algorithm

4.4.1. Shift of Observation Time

The most accurate results in terms of time resolution can be achieved by applying the detector to every new sample that is collected from the ground station's antenna, which corresponds to a shift of observation time by $\theta_{shift} = 1$ sample. In this case, the time resolution is considered to be the observation time T. This results from the fact that the cyclic feature estimation applies averaging over one observation time, the exact timing of events happening within one observation time can not be recovered. However, this is not feasible to compute on common hardware in real time. A shift parameter θ_{shift} must be introduced, which defines a trade-off between time resolution and computational tractability. For the final detector, a choice of $\theta_{shift} = \frac{T}{8}$ was found to perform well.

Example: In correspondence to the block length example in Section 4.2.3, the Doppler rate is chosen to be $8\frac{kHz}{s}$ *for this demonstration. Also, the block length parameter is set to be* $\epsilon = 0.5$. *Figure 4.12 shows only a part of Figure 4.11, where multiple blocks are marked as* B_i, B_j, B_k, *each shifted by* $\delta_{shift} = \frac{T}{8}$.

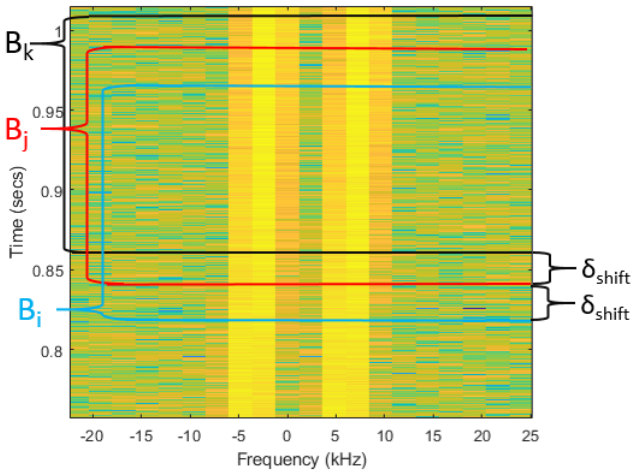

Figure 4.12.: Graphical Illustration of δ_{shift}

The block length is limited by the Doppler rate. For the actual PropCube signal, a choice of $\epsilon = 0.5$ and $\delta_{DR} = 310\frac{Hz}{s}$ results in a observation time of around $T = 0.155s$. With overlapping due to $\theta_{shift} = \frac{\Delta T}{8}$, there are 43 observation times for each burst of length $1s$, where the burst is fully present.

Hence, it is highly likely to achieve multiple detections for each burst. Various strategies can be construed to increase the overall reliability, for example by assuming the presence of a burst only if more detections are yielded than a defined threshold. Therefore, a single false alarm would be discarded. Moreover, false-positives can easily be spotted as outliers, when a frequency change greater than physically possible is measured. However, as demonstrated in Chapter 5, it is possible to chose the parameter settings in a way that no false-positives occurred in all the testing done for this thesis, while detections in multiple neighboring observation times guarantee a reliable detection of each burst. Therefore, it was not necessary to remove outliers by post processing or introduce a new thresholds. Figure 4.15 depicts multiple detection points, each corresponding to one observation time, which belong all together to the same burst.

The overall execution for a data recording of 227 seconds can be managed on a standard desktop computer, which was used for the development in this thesis, in as little as 10 seconds. Of course, this is not a proper execution time analysis, but it is mentioned to imply that real-time applications are possible. However, a short time delay is introduced by applying frequency corrections after receiving entire bursts only, as described in the next Section.

4.4.2. Frequency Correction

As described in Section 4.4.1, there are multiple observation times for each burst, leading to multiple possible detection points. For each detection point, the position of

the cyclic feature in the α-slice yields the Doppler shift. The change of Doppler shift from detection point to detection point reveals the Doppler rate. In this thesis, a linear interpolation of those points is proposed to be used as a frequency correction curve. Although the Doppler rate is rarely as high as $310\frac{Hz}{s}$ and changes continuously, a constant value was found to be a sufficient approximation for the Doppler rate for intervals as short as one second. After isolating a burst in time domain, the frequency correction is performed. Afterwards, out of band noise is filtered to improve the SNR. The processed burst is then passed on to the demodulator. Figure 4.13 illustrates the processing flowgraph, whereas the following example demonstrates the processing steps on real-world data.

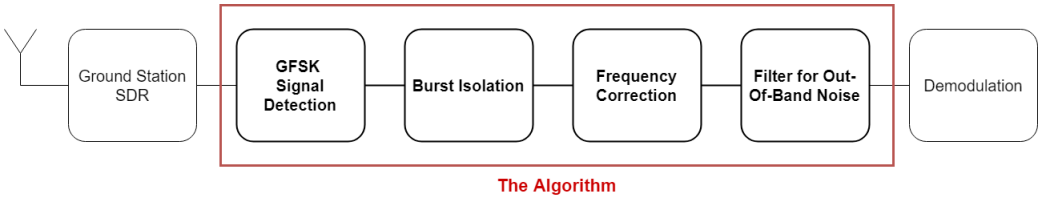

Figure 4.13.: Processing Flowgraph

Example: Figure 4.14 shows a burst in the ISM band. For the sake of a clear demonstration, a burst was chosen, which was received when the satellite was close to the ground station, resulting in a relatively high SNR and a high Doppler rate. The detections points and their corresponding Doppler shift estimation are presented in Figure 4.15. After one burst is received, the detection points are interpolated linearly, which is depicted by the red line in Figure 4.15.

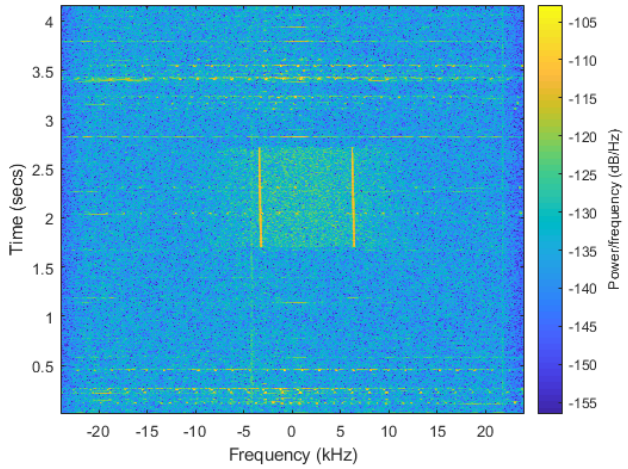

Figure 4.14.: Burst as received at Ground Station SDR

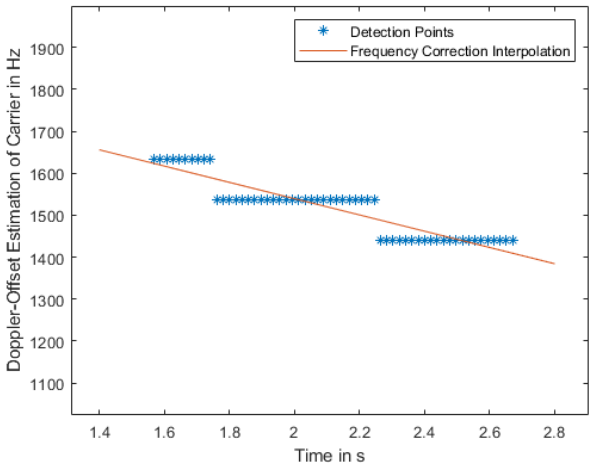

Figure 4.15.: Interpolated Detection Points

In the further processing, the burst is cut out in time domain with a slight tolerance before the first and after the last detection point. The final product after frequency correction and filtering is shown in Figure 4.16.

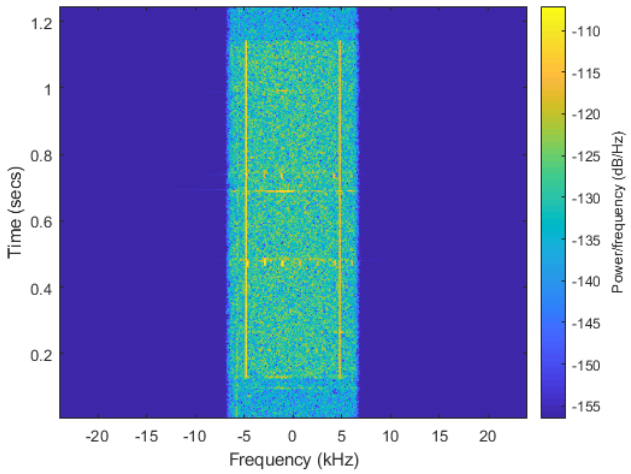

Figure 4.16.: Isolated, frequency-corrected and filtered burst

5. Detector Performance

The performance analysis was conducted with the parameter settings proposed in Table 5.1 and 5.2.

As a performance benchmark, it is desirable to determine the performance in a WGN environment. Since it is not tractable to give analytic expressions, exhaustive simulations were performed in Section 5.2. Moreover, it is interesting to evaluate how the detector's performance degrades in the ISM environment. Obviously, it is impossible to model ISM bands, because those are highly non-stationary and unpredictable. Therefore, simulations are complicated. However, in Section 5.3 an approach was taken, which uses a recorded ISM background to perform simulations and provide a ROC. Most importantly, the effectiveness of the detector is eventually tested on real-world data of a PropCube overflight in Section 5.4.

5.1. Parameter Settings

While some parameters are defined by the system design or physical circumstances (Table 5.1), there is a variety of parameters free to be determined (Table 5.2). Many justifications for those parameter choices were given in the previous chapters.

5.1.1. Given Parameters

Table 5.1 presents the parameters given by the system design or physical circumstances.

Description	Parameter	Value
Symbol-Rate $[\frac{symbols}{s}]$	f_{symb}	9600
Maximum Doppler Rate $[\frac{Hz}{s}]$	δ_{DR}	310
Center Frequency $[MHz]$	f_0	914
Bandwidth-Time-Product	BT	0.5
Modulation-Index	h	1

Table 5.1.: Parameters given by system design

5.1.2. Proposed Parameters

Table 5.2 presents the parameter settings proposed in this thesis. By empirical studies, those were found to perform best, coping with all the implications arising from the

thesis' application, like a variable SNR-range and interference in the ISM environment. For a detailed discussion of each parameter, the reader is referred to Chapter 4.

A threshold-parameter of $\kappa = 0.12$ is very conservative, because it leads to a false-positive probability very close to zero. No false-positives were detected with $\kappa = 0.12$ in all the testing conducted for this thesis. However, the probability of detection is still sufficient to achieve multiple detections for each burst. An overall proof for the detectors reliability and a detailed performance analysis is provided in Section 5.4.

Description	Parameter	Value
Sampling-Rate [kHz]	f_{sample}	48
DFT Length [bins]	N	500
Block length [samples]	B	7432
Number of Sub-blocks	M	15
Threshold	κ	0.12
Max. Doppler Smearing per B [DFT bin width]	ϵ	0.5
Shift of Observation Times	θ_{shift}	$\frac{B}{8}$

Table 5.2.: Parameter settings proposed in this thesis

5.2. Performance in WGN

In a WGN environment, no false-positives were detected for threshold parameters as high $\kappa = 0.5$. In a more vivid manner, this can be interpreted that no frequency components separated by $\alpha = 9.6kHz$ could be found in WGN, which exhibit $\frac{1}{\kappa}$ times the spectral correlation than combinations of all other components. While zero is a true result for the false-positive probability for observation times approaching infinity, the false-positive probability in this application can not be equal to zero, since the observation time is limited. However, despite exhaustive simulations, no false-positives were detected in a WGN environment for values of κ, which are reasonable to use in an ISM environment, i.e. $\kappa \leq 0.5$. Often, the ROC is presented as a plot of the true-positive probability over the false-positive probability. Due to the low false-positive probability, this would appear to be very close to an optimum ROC. A more meaningful plot can be provided by depicting the true-positive probability for a range of SNRs.

A simulator was built, which inserts GFSK bursts similar to PropCube's signal into a stationary WGN environment of variance $\sigma_n = 1$. The signal power σ_s can be chosen arbitrarily, to simulate the detection behaviour at any SNR. Consequently, the SNR is defined by

$$SNR = 10 \times \log_{10}\left(\frac{\sigma_s}{\sigma_n}\right). \tag{5.1}$$

A burst has a length of one second, corresponding to 48×10^3 samples at a sampling rate of $48kHz$. Additionally, each burst was manipulated to have the worst-case Doppler rate of $310\frac{Hz}{s}$. Then, the algorithm described in Section 4.4 was used to detect the bursts. A detection is only considered to be possible, if the burst is present in the entire observation time. After a run of 10^5 possible detections per SNR, it was validated that no false-positives were present. Hence, the true-positive rate could be calculated by evaluating the ratio of true-positives to all possible detections. The results are depicted in Figure 5.1. Again, it is mentioned that the probability of detection reflects the probability of detection in one observation time, whereas 43 observation times are contained in each PropCube burst.

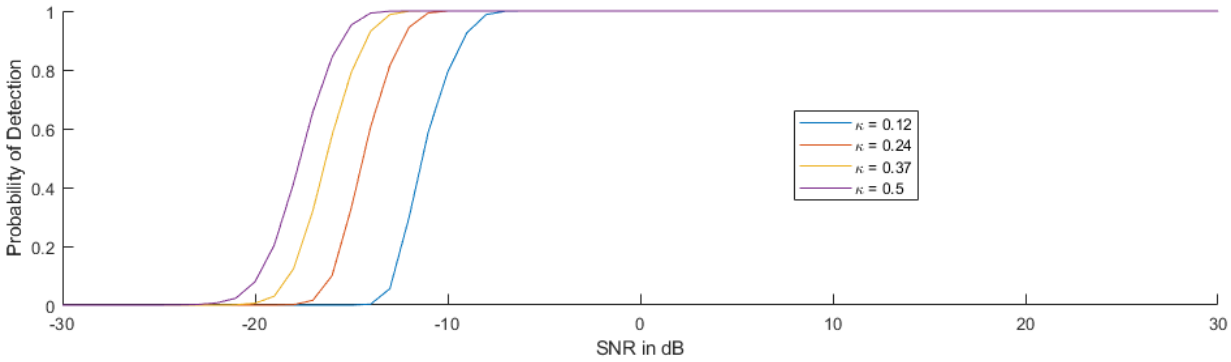

Figure 5.1.: Detector Performance in WGN Environment

5.3. ISM-Band Simulation

The ISM band is a highly non-stationary environment: Depending on location, time, weather and multiple other factors, the appearance of interference changes drastically. When testing the detector in practice, the only chance to obtain the receiver operating characteristic would be to mark missed detections and false-positives by hand, assuming the signal can be recognized by humans, for example in a spectrogram plot. Since this is not traceable, another approach was taken: The $914MHz$ ISM band was recorded when it was known that no PropCube satellite was over the NPS ground station in Monterey, CA. Then, the algorithm was used to obtain false-positives for various thresholds: Since the absence of PropCube's signal is guaranteed, any detection corresponds to a false-positive. The false-positive rate was determined later by the ratio of false-positives to possible detections. The recording is modeled to contain two components: White Gaussian noise with power σ_n and interference with power σ_I. Figure 5.2 shows a time series of the magnitude of the first 4 seconds of the recorded ISM background.

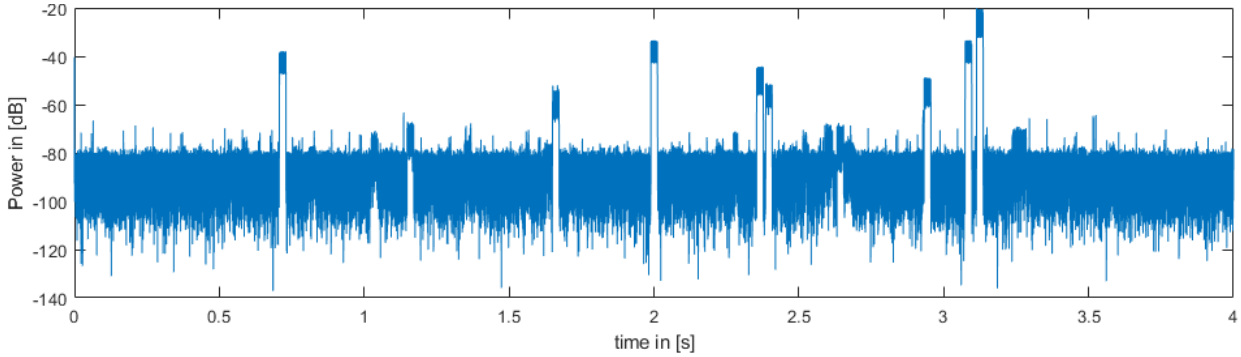

Figure 5.2.: Magnitude of recorded ISM background

The SNR values in Figure 5.3 take only σ_n into account, since σ_I is highly non-stationary. The power of the WGN background was measured with methods presented in Appendix A, when interference appeared to be absent. Then, analog to Section 5.2, GFSK bursts could be inserted and the performance could be evaluated. Again, the true-positive rate was determined by the ratio of true-positives to all possible detections. The results are depicted in Figure 5.3.

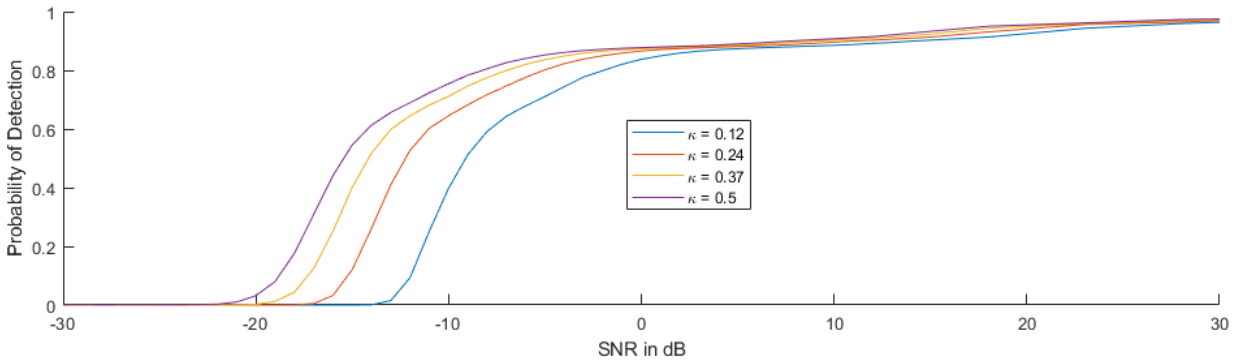

Figure 5.3.: Detector Performance in ISM Environment

Since the power of interference σ_I is not considered in the SNR values, a degradation of performance compared to Figure 5.1 can be observed. Moreover, Figure 5.3 shows an asymptotic behaviour of the probability of detection, which slowly approaches 1. This leads to the interpretation that even at high choices of σ_s few interferers cause an erraticism in the α-slice exceeding the threshold T_{AS}. This is reasonable since occasionally σ_I exceeds σ_s greatly and the observation time is limited by the Doppler rate and the block length parameter ϵ. Additionally, interference, that actually exhibits cyclic features at a cycle frequency of $\alpha = 9.6kHz$ could cause missed detections of PropCube's signal. However, since 43 observation times fall into the length of each burst, the detection probability of a burst is much higher, so that the presence of every burst could be detected.

The false-positive rates for each threshold, which were estimated with the previously described method, are presented in table 5.3.

κ-Value	False-Positive Rate
0.12	0
0.24	3.7×10^{-4}
0.37	3.3×10^{-3}
0.5	1.4×10^{-2}

Table 5.3.: Estimated False-Positive Rates for various Threshold Parameters κ

Again, it is to be mentioned that this approach is not representative and the receiver operating characteristic in the ISM band heavily relies on multiple factors, which are difficult to model.

5.4. Real-World Performance

After all, the detector's performance must be evaluated in the practical application. Figure 5.4 shows the detection results for an overflight by a PropCube satellite. It can easily be seen that no outliers are present, which leads to the conclusion that the false-positive rate can assumed to be zero for this overflight. By detecting bursts at various SNRs during this overflight, the effectiveness of the adaptive decision statistic is demonstrated.

In Figure 5.4, a total of 1336 detections was made for 36 transmitted bursts, resulting in an average of 37.1 detection points per burst out of a maximum of 43 possible detections. The overall effectiveness of the proposed detector can also be stated by comparing it to a radiometer based approach as presented in Appendix B, which was conducted with the same data.

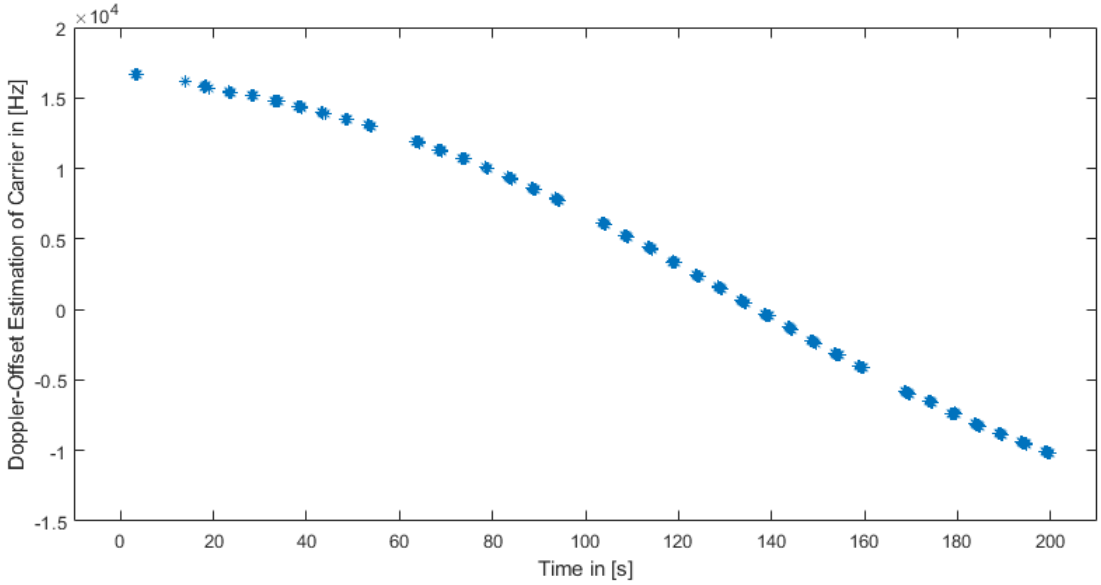

Figure 5.4.: Detectors Real-World Performance during a PropCube Overflight

6. Conclusions

This thesis successfully demonstrates that cyclic spectral analysis can be applied to signals corrupted by Doppler rate as high as $310\frac{Hz}{s}$. The benefits of this framework, namely its tolerance against interference, can be exploited to reliably detect the presence of LEO satellite signals operating in the ISM band. Compared to conventional methods, like a radiometer as presented in Appendix B, the false-positive rate could be lowered significantly. In fact, it could be achieved to detect every burst multiple times while no false-positives occurred. Moreover, frequency correction can be performed with an accuracy at least as high as the DFT resolution because the positions of cyclic features shift slowly as the algorithm is applied to a stream of incoming sampling data. Each detection point reveals the instantaneous Doppler shift, whereas an interpolation of many detection points is shown to be an effective tool to estimate and correct the Doppler rate. Eventually, each burst is separated in time domain, filtered to remove out-of-band noise and passed on to the demodulator.

Additionally, this thesis demonstrates that a standard single-cycle detector needs to be modified to work reliably in the ISM environment. Multiple detection statistics are discussed before an adaptive detection statistic, which is able to cope with variations in the signal power, is proposed. The design of the detection statistic is motivated by the shape of the ideal α-slice, which is derived in this thesis from [4].

Eventually, a performance analysis is conducted, which presents the probability of detection for different scenarios. The ultimate test, the real-world performance, proves the effectiveness of the proposed detection algorithm.

Bibliography

[1] C. M. Spooner. Cyclostationary Signal Processing - UNDERSTANDING AND USING THE STATISTICS OF COMMUNICATION SIGNALS. https://cyclostationary.blog/. Accessed: May 09, 2019.

[2] W. A. Gardner. *Statistical Spectral Analysis - A Nonprobabilistic Theory*. McGraw-Hill, 1987. ISBN 0-13-844572-9.

[3] W. A. Gardner and C. M. Spooner. Signal Interception: Performance Advantages of Cyclic-Feature Detectors. *IEEE TRANSACTIONS ON COMMUNICATIONS*, Vol. 40(8), January 1992.

[4] A. Napolitano and C. M. Spooner. Cyclic Spectral Analysis of Continuous-Phase Modulated Signals. *IEEE TRANSACTIONS ON SIGNAL PROCESSING*, Vol. 49(1), January 2001.

[5] J. G. Proakis. *Digital Communications*. McGraw-Hill, 4 edition, 2001. ISBN 0-07-232111-3.

[6] C. M. Spooner. *Theory and Application of Higher-Order Cyclostationarity*. PhD thesis, UNIVERSITY OF CALIFORNIA DAVIS, June 1992.

[7] W. A. Gardner. *Introduction to Random Processes with Applications to Signal*. McGraw-Hill Inc., 2 edition, 1990. ISBN 0-07-022855-8.

[8] W. A. Gardner, W.A. Brown, and C.-K. Chen. Spectral Correlation of Modulated Signals: Part II-Digital Modulation. *IEEE TRANSACTIONS ON COMMUNICATIONS*, Vol. COM-35(6), June 1987.

[9] W.A. Brown, H.H. Loomis, and R. S. Roberts. Computationally Efficient Algorithms for Cyclic Spectral Analysis. *IEEE Signal Processing Magazine*, Vol. 41(2), April 1991.

[10] W. A. Gardner and C. M. Spooner. The Cumulant Theory of Cyclostationary Time-Series, Part II: Development and Applications. *IEEE TRANSACTIONS ON SIGNAL PROCESSING*, Vol. 42(12), December 1994.

[11] W. A. Gardner. Signal Interception: A Unifying Theoretical Framework for Feature Detection. *IEEE TRANSACTIONS ON COMMUNICATIONS*, Vol. 36(8), August 1988.

[12] J. Whisart and M. S. Bartlett. The distribution of second order moment statistics in a normal system. *Proceedings of the Cambridge Philosophical Society XXVIII*, 1932.

[13] A. Papoulis and S. U. Pillai. *Probability, Random Variables, and Stochastic Processes*. McGraw-Hill, 4 edition, 2002.

A. Example Spectrograms and SNR Estimation

A.1. Example Spectrograms of typical Bursts

Figures A.1 and A.2 illustrate the challenging environment, which the ISM band poses on the communication link of PropCube. The two straight tones in each figure, lasting for about one second, represent the upper and the lower frequency of PropCube's GFSK signal. Various, much stronger interferers can be observed across the spectrogram. The different center frequencies are a result of the Doppler shift, and also the Doppler rate can be observed, especially in Figure A.1 as a slight frequency shift happening within the signal. The sampling rate was set to $48kHz$ and a DFT of length 1024 was used to calculate the spectrograms.

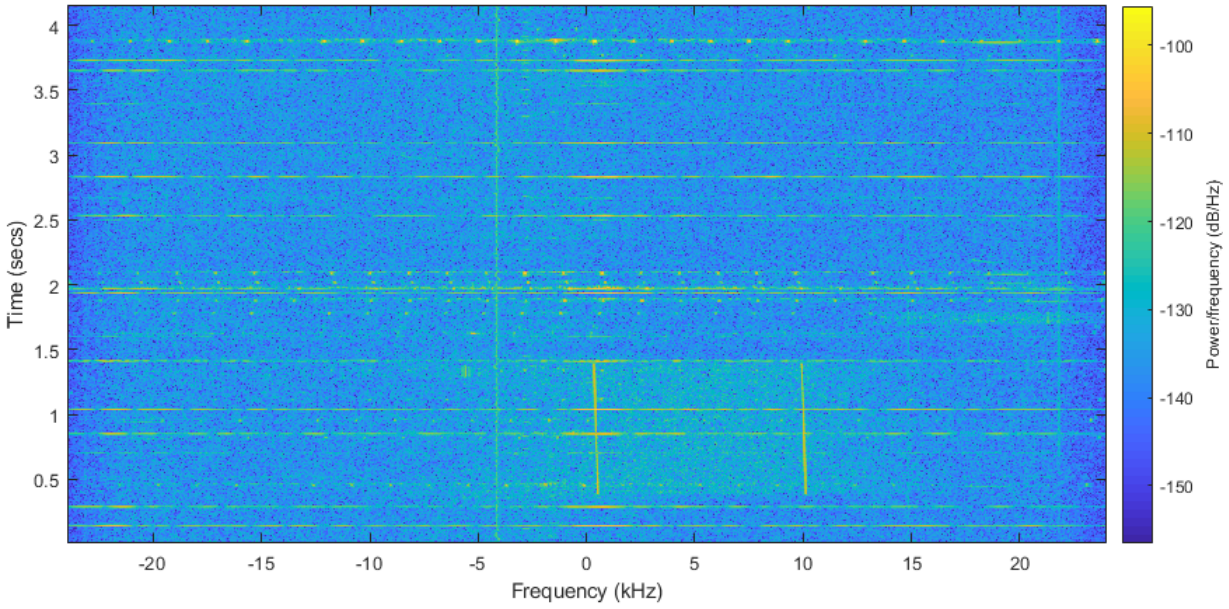

Figure A.1.: PropCube Burst centered around $5kHz$ from $0.4s$ to $1.4s$

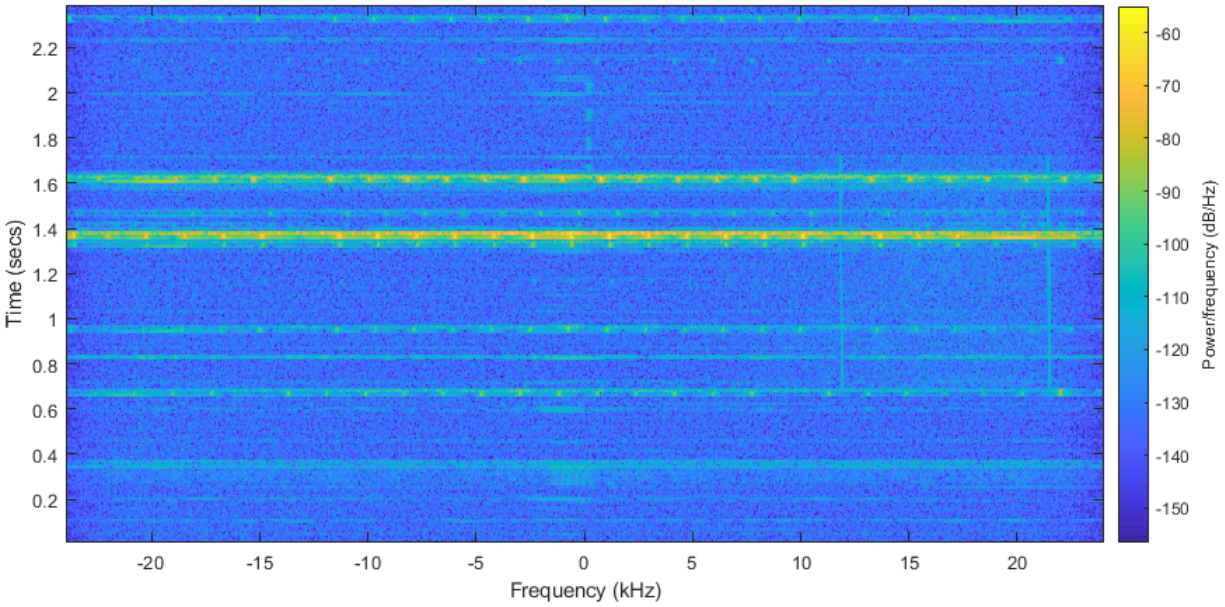

Figure A.2.: PropCube Burst centered around $17kHz$ from $0.7s$ to $1.7s$

A.2. SNR Estimation

In this section, a coarse estimation of SNR is conducted. Since the satellite's signal consists not only of the two tones, which are clearly visible, but also of a lobe-like component, it is difficult to apply a histogram based method. The estimation used here is a simple comparison of energies when there is signal present or when not. It is assumed that the noise floor can be modeled as stationary additive WGN and interference, which significantly influences the SNR estimation, can be identified in the spectrogram plot. For example, Figure A.3 is considered to be free of interference and therefore represent a burst in WGN environment, whereas the obvious interferer in Figure A.4 could be used in Section A.2.2 to estimate the SNR when interferers are present.

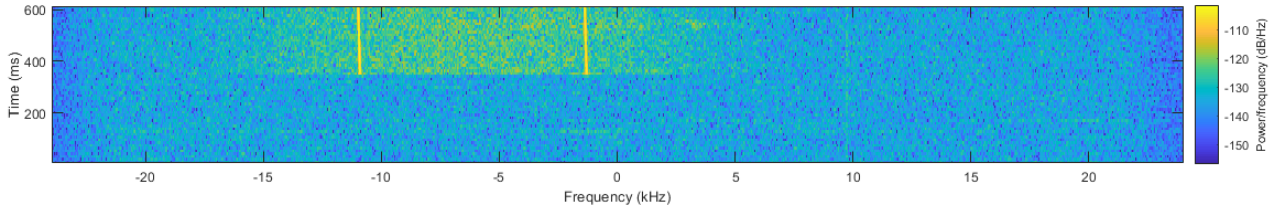

Figure A.3.: Part of Signal Burst, which is assumed to be in WGN environment

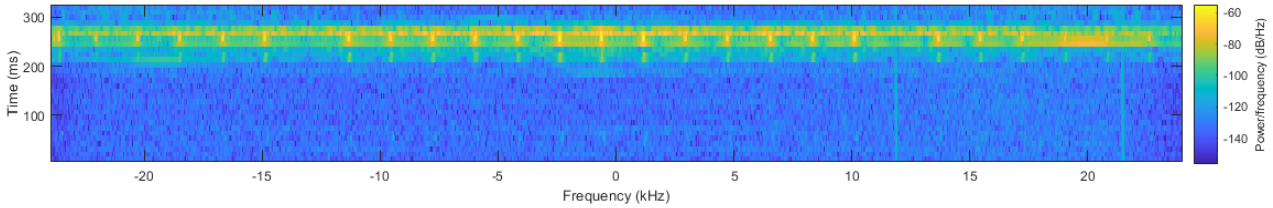

Figure A.4.: Strong Interferer in Burst Part

A.2.1. SNR Estimation in AWGN Background

Since the signal power varies greatly due to the difference in range from the satellite to the ground station, this SNR estimation is performed for two different scenarios. First, to estimate the lower bound of the SNR range, a burst in the very beginning of an overflight was chosen and secondly, to get an upper bound, a burst transmitted very close to the ground station was chosen. The following steps were performed on a sampling sequence like Figure A.3, where interference seems to be absent:

- The total energy $E_{s,n}$ of the 5000 samples, where satellite signal is embedded in an AWGN background, is computed
- The total energy E_n in the 5000 samples, where no satellite signal but only the AWGN background is present, is computed
- The difference of both yields the Signal Power $E_s = E_{s,n} - E_n$
- The logarithmic representation of $\frac{E_s}{E_n}$ yields the SNR

The range for the SNR in an AWGN background was determined to be from $-2dB$ to $13dB$.

A.2.2. SNR Estimation with strong Interference

To estimate the SNR, which can occur when strong interference is present, a burst part was chosen where a very strong interferer overlaps with the satellites signal. Then the following calculations are performed:

- 1250 samples, which contain the interferer, are separated
- The energy $E_{s,n,inf}$, which consists of the energy of the interferer, the satellite signal and AWGN, is computed and multiplied by a factor $\frac{5000}{1250}$
- The energy of the Interferer E_{inf} is calculated by subtraction of the energies previously estimated in Section A.2.1: $E_{inf} = E_{s,n,inf} - E_s - E_n$
- The logarithmic representation of $\frac{E_s}{E_n + E_{inf}}$ yields the SNR

Multiple estimations of various, strong interferes yield SNR values as low as $-37dB$.

B. Radiometer

To evaluate the possibilities of conventional spectral analysis and further to motivate cyclostationary methods, a radiometer was implemented. This appendix is not meant to provide a detailed radiometer evaluation and its thresholds, but is rather designed to show the qualitative differences in comparison to Figure 5.4 and Section 5.4 of the detector proposed in this thesis. Analog to the final algorithm described in Section 4, the same block length of $B = 7432$ samples was used to avoid smearing in the frequency domain, as well as a shift of observation-times by $\theta = \frac{B}{8}$. Instead of using multiple estimations of cyclic periodograms to calculate an α-slice, the radiometer estimates one conventional periodogram for each block length. Then, it searches for frequency components separated by $9600kHz$, which contain energy above a certain threshold. The frequency components were defined as small frequency ranges of width $\delta_{DR} \times \epsilon$, to take residual smearing into account. The same data used for the real-world performance evaluation in Section 5.4 was used to test the radiometer. Figures B.2 and B.1 show the dilemma of energy detection: If the energy threshold is chosen low enough to make at least two detections per burst (Figure B.1), the false-positive rate was approximated to be $P_{fp} = 0.6$, whereas a higher threshold, corresponding to a false-positive rate of $P_{fp} = 0.23$, already misses many bursts (Figure B.2).

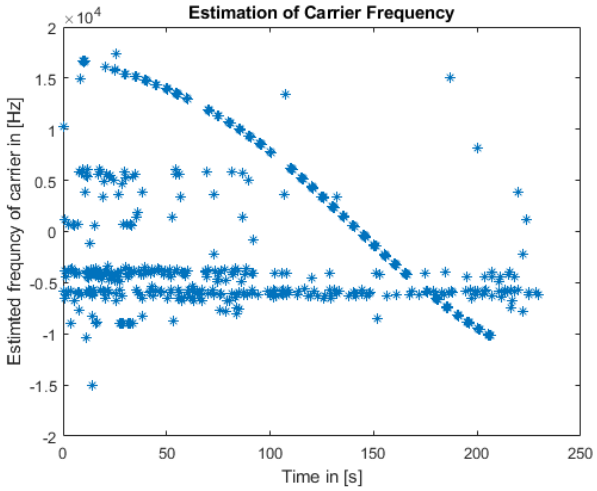

Figure B.1.: Detection Points for a low threshold

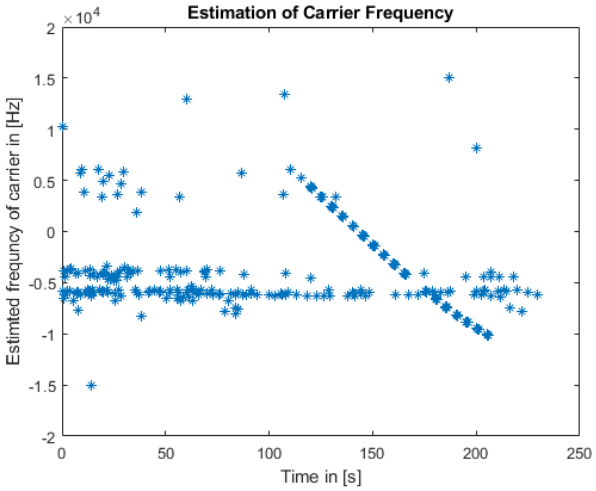

Figure B.2.: Detection Points for a high threshold

Of course, many modifications can be taken to improve the performance of conventional radiometers. However, its basic functional principle to solely rely on the pres-

ence of energy in certain frequency bands can not be changed. Therefore, other detection strategies, like cycle-detectors, are a more promising approach in the context of this thesis.

C. Phase Compensation Factor

The SCF estimate of the TSM can be expressed as

$$\hat{S}_x^\alpha(f) = \frac{1}{M}\sum_{m=0}^{M-1}\left[\hat{I}_N^\alpha(k+mN,f)\right] \tag{C.1}$$

and thus can be interpreted as the average over all cyclic periodogram estimates $\hat{I}_N^\alpha(k+mN,f)$. The parameter k is the time discrete representation of t in 2.12 and mN is the shift of the mth cyclic periodogram as the algorithm slides through the entire sample data. Since each cyclic periodogram is calculated by using a single, independent Fourier transform, the information of the shift by mN samples of the cyclic periodograms relative to each other is lost. By inspecting the formulas, it can be seen most clearly when inserting the definition of the cyclic periodogram in discrete time

$$\hat{I}_N^\alpha(k+mN,f) = \frac{1}{N}\hat{X}_N(k+mN,f+\alpha/2)\hat{X}_N^*(k+mN,f-\alpha/2) \tag{C.2}$$

where $\hat{X}_N(k+mN,f+\alpha/2)$ is N-point discrete Fourier transform of $x(k+mN)$. Assuming that f and α are provided in a normalized manner, i.e. $fN \in \mathbb{Z}$ and $\alpha T \in \mathbb{Z}$ corresponding to the TSM's spectral and cyclic resolution [9], the calculation can be performed by evaluation of

$$\hat{X}_N\left(k+mN,f+\frac{\alpha}{2}\right) = \sum_{n=0}^{N-1} x(n+mN)e^{-i2\pi(f+\frac{\alpha}{2})(n+mN)}. \tag{C.3}$$

Simply applying a N-point Fourier transform to the shifted data blocks only yields

$$\sum_{n=0}^{N-1} x(n+mN)e^{-i2\pi(f+\frac{\alpha}{2})n}, \tag{C.4}$$

which makes it obvious that a phase error is introduced. In order to still obtain a correct estimation, it is necessary to compensate for the neglected shift by multiplying a phase compensation factor. This can be done for each point of the discrete Fourier transform, by multiplying

$$e^{(-i2\pi(f+\frac{\alpha}{2})mN)}. \tag{C.5}$$

Alternatively, the phase compensation can be performed at a later step by multiplying the phase compensation factor

$$e^{(-i2\pi\alpha mN)}. \tag{C.6}$$

to each cyclic periodogram.

In the special case, when $\alpha = \frac{k}{N}, k \in \mathbb{Z}$, the phase compensation factor is always equal to unity and can therefore be ignored. In this thesis, the desired cycle frequency was known a-priori and all parameters were eventually chosen in a way that the phase compensation factor is not necessary. However, if the cycle frequencies are not known a-priori and a full spectral analysis, i.e. for all cycle frequencies $\alpha = \frac{k}{T}, k \in \mathbb{Z}$, must be conducted, the application of the phase compensation factor is crucial.

D. Pairwise Uncorrelatedness of DFT Bins of WGN

For the derivation of the output statistics of a TSM estimator, it is necessary to show that output DFT bins $X(k_i)$ and $X(k_j)$ are uncorrelated for $i \neq j$ if only WGN is applied.

Two random variables X and Y are uncorrelated, if

$$cov\{X, Y\} = E\{XY\} - E\{X\}E\{Y\} = 0 \tag{D.1}$$

holds. Using the definition of the DFT, X and Y are defined by

$$X = \sum_{n=0}^{N-1} x(n) e^{-i2\pi k_i \frac{n}{N}} \tag{D.2}$$

and

$$Y = \sum_{n=0}^{N-1} x(n) e^{-i2\pi k_j \frac{n}{N}}. \tag{D.3}$$

It can be shown easily that

$$E\{X\} = E\{Y\} = 0. \tag{D.4}$$

Therefore, equation D.1 simplifies to

$$cov\{X, Y\} = E\{XY\} = 0. \tag{D.5}$$

Inserting the definition of X and Y, it follows that

$$E\{XY\} = E\left\{ \sum_{n=0}^{N-1} x(n) e^{-i2\pi k_i \frac{n}{N}} \sum_{n=0}^{N-1} x(n) e^{-i2\pi k_j \frac{n}{N}} \right\}, \tag{D.6}$$

which can be expanded to

$$E\{XY\} = E\{x(0)x(0)e^{-i2pi(k_i+k_j)\frac{0}{N}}\} + E\{x(0)x(1)e^{-i2pi(k_i+k_j)\frac{1}{N}}\} + ... + E\{x(N-1)x(N-1)e^{-i2pi(k_i+k_j)\frac{N-1}{N}})\}. \tag{D.7}$$

Now, the expression is a sum, which allows to pull the expectation operator inside. The complex exponential is a deterministic factor and can be written in front of the

expectation operator. The right side of equation D.7 is composed of two different kinds of terms:

$$I. : \epsilon_{e,f} E\{x(e)x(f)\}, \qquad e \neq f, \tag{D.8}$$

where $\epsilon_{e,f}$ is a complex exponential and

$$II. : e^{-i2\pi k' \frac{e}{N}} E\{x(e)x(e)\}, \tag{D.9}$$

where $k' = k_i + k_j$. For I. it holds that

$$\epsilon_{e,f} E\{x(e)x(f)\} = \epsilon_{e,f} E\{x(e)\}E\{x(f)\} = 0 \tag{D.10}$$

since x(e) and x(f) are uncorrelated and zero-mean by definition of WGN. Taking all terms of II. into account, the equation D.1 can be expressed as

$$cov\{X,Y\} = \sum_{e=0}^{N-1} e^{-i2\pi k' \frac{e}{N}} E\{x(e)x(e)\} = \sum_{e=0}^{N-1} e^{-i2\pi k' \frac{e}{N}} E\{x(e)^2\} = \sum_{e=0}^{N-1} e^{-i2\pi k' \frac{e}{N}} \sigma_n^2, \tag{D.11}$$

which can be interpreted as the Fourier transform of a constant, namely the variance of WGN. It is well known that the DFT of a constant for $k' \neq 0$ yields zero:

$$\sum_{e=0}^{N-1} e^{-i2\pi k' \frac{e}{N}} \sigma_n^2 = 0, \qquad k' \neq 0. \tag{D.12}$$

Eventually, it follows that

$$cov\{X,Y\} = E\{XY\} = 0. \tag{D.13}$$

Hence, distinct output bins of a DFT are pairwise uncorrelated.